JGR Oceans

RESEARCH ARTICLE
10.1029/2020JC016637

Aquatic Biogeochemical Eddy Covariance Fluxes in the Presence of Waves

Matthew H. Long[1]

[1]Marine Chemistry and Geochemistry Department, Woods Hole Oceanographic Institution, Woods Hole, MA, USA

Key Points:

- Literature review of eddy covariance studies reveals many studies were conducted in shallow waters where waves bias measurements
- Sampling higher above the boundary shifts turbulence to longer scales, producing a spectral gap between wave and turbulent frequencies
- A change in how studies are conducted and analyzed will enable the removal of wave bias and new chemical tracer applications

Supporting Information:

- Supporting Information S1
- Table S1

Correspondence to:
M. H. Long,
mlong@whoi.edu

Citation:
Long, M. H. (2021). Aquatic biogeochemical eddy covariance fluxes in the presence of waves. *Journal of Geophysical Research: Oceans*, *126*, e2020JC016637. https://doi.org/10.1029/2020JC016637

Received 22 JUL 2020
Accepted 12 JAN 2021

Abstract The eddy covariance (EC) technique is a powerful tool for measuring atmospheric exchange rates that was recently adapted by biogeochemists to measure aquatic oxygen fluxes. A review of aquatic biogeochemical EC literature revealed that the majority of studies were conducted in shallow waters where waves were likely present, and that waves biased sensor and turbulence measurements. This review identified that larger measurement heights shifted turbulence to lower frequencies, producing a spectral gap between turbulence and wave frequencies. However, some studies sampled too close to the boundary to allow for a spectral turbulence-wave gap, and a change in how EC measurements are conducted and analyzed is needed to remove wave-bias. EC fluxes have only been derived from the time-averaged product of vertical velocity and oxygen, often resulting in wave-bias. Presented is a new analysis framework for removing wave-bias by accumulation of cross-power spectral densities below wave frequencies. This analysis framework also includes new measurement guidelines based on wave period, currents, and measurement heights. This framework is applied to sand, seagrass, and reef environments where traditional EC analysis resulted in wave-bias of 7.0% ± 9.2% error in biogeochemical (oxygen and H^+) fluxes, while more variable and higher error was evident in momentum fluxes (10.5% ± 21.0% error). It is anticipated that this framework will lead to significant changes in how EC measurements are conducted and evaluated, and help overcome the major limitations caused by wave-sensitive and slow-response sensors, potentially expanding new chemical tracer applications and more widespread use of the EC technique.

Plain Language Summary Biogeochemical processes can be estimated by the exchange of vital tracers between the seafloor, overlying water, and the atmosphere and are paramount to understanding global biogeochemical cycling. Techniques that measure water transport and tracers of these processes (here oxygen and pH) have revolutionized how these exchanges are studied, and how they impact local water quality, productivity, and nutrient cycling. Through measurements of oxygen concentration and pH, and their transport by water movement, their exchange can be determined. These techniques were originally developed to examine exchange between the land and atmosphere, but applying these techniques to aquatic ecosystems has presented challenges due to surface waves that are present in the shallow aquatic ecosystems where these aquatic techniques are commonly applied. Waves cause errors in the sensors used to measure water transport and tracer concentrations, and have presented significant challenges for applying these atmospheric techniques underwater. This research presents new guidelines for these aquatic exchange measurements that will require a change in how measurements are conducted and analyzed, to allow for tracer exchange measurements in the presence of waves. These new guidelines also allow for new sensors that were previously incompatible, expanding the applications of these techniques to new scientific research questions.

1. Introduction

Eddy covariance (EC) and related boundary layer exchange techniques have been used in terrestrial ecosystems since the early 1950s to measure fluxes of water and heat (Swinbank, 1951) and are widely applied today to measure a variety of biogeochemical and energy fluxes in the atmospheric boundary layer (e.g., Baldocchi, 2003; Burba & Anderson, 2010; Lee et al., 2004). The physical oceanography community has applied this atmospheric boundary layer theory to fluxes of momentum, heat, and salt in marine settings, where waves have been identified as a unique source of bias in oceanic turbulence measurements (Scully et al., 2016; Trowbridge, 1998; Trowbridge et al., 2018). The application of boundary layer theory to aquatic

biogeochemical fluxes is comparatively new, and has mainly been used to examine oxygen (O_2) fluxes as a proxy for carbon exchange.

The aquatic EC technique measures the flux of solutes between the benthic surface and the overlying water (Berg et al., 2003; Lorrai et al., 2010; Reimers et al., 2012). EC measurements are widely considered the most reliable flux method because they require the fewest physical assumptions (Fairall et al., 2000). The aquatic EC technique has been used in challenging environments, where traditional methods are difficult to apply, such as benthic macrophytes (Hume et al., 2011; Koopmans et al., 2020), sea-ice (Glud et al., 2014; Long et al. 2012a), lakes (Brand et al., 2008; McGinnis et al., 2008), rocky substrates (Attard et al., 2019; Glud et al., 2010), oyster beds (Reidenbach et al, 2013; Volaric et al., 2018), the deep sea (Berg et al., 2009; Donis et al., 2016), and coral reefs (Long et al., 2013, 2019; Rovelli et al., 2015) and represents a highly advantageous methodology for examining high-temporal resolution, ecosystem-level fluxes in complex environments. The aquatic EC technique has been occasionally applied to other tracers including temperature (Crusius et al., 2008; Else et al., 2015; Long et al., 2012a), salinity (Crusius et al., 2008), nitrate (Johnson et al., 2011), hydrogen sulfide (McGinnis et al., 2011) and pH (Long et al., 2015a). The aquatic EC technique has also been applied to the atmosphere-water interface to measure atmospheric O_2 exchange (Berg & Pace, 2017; Long & Nicholson 2018) and at the oxycline and thermoclines in lakes (Kreling et al., 2014; Weck & Lorke, 2017).

The basis for the EC technique is that turbulent mixing, caused by the interaction of current velocity with the benthic, atmospheric, sea-ice, or cline interfaces, is the dominant vertical transport process in boundary layers. Therefore, vertical fluxes across the ecosystem interfaces can be derived from high temporal resolution measurements of the vertical velocity and a solute concentration. The time-averaged EC flux across an interface are determined by:

$$Flux = \overline{w'c'} \tag{1}$$

where the overbar represents a time average, and w' and c' are the fluctuating components of the vertical velocity and scalar concentration (c), respectively, that are measured at the same point at a fixed distance away from the interface.

Recent work has highlighted the influence of wave and current variability on EC measurements (Berg et al., 2015; Donis et al., 2015; Holtappels et al., 2015; Reimers et al., 2016a) when applying the most commonly used sensor in aquatic EC measurements, the Clark-type O_2 microsensor (Revsbech, 1989). Studies demonstrating wave bias have indicated that automated numerical time-lag corrections (for slow or spatially separated sensors) can be biased by wave orbital motion (Berg et al., 2015; Donis et al., 2015), that cospectral analysis reveals significant contributions to fluxes at wave frequencies (Kuwae et al., 2006; Long et al., 2015b; Reimers et al., 2016a), and that Clark-type oxygen sensors can be biased by zero-crossing wave velocities (Holtappels et al., 2015; Reimers et al., 2016a). These Clark-type microsensors have been designed to limit "stirring sensitivity" by reducing the tip size and microsensor design, but trade-offs exist between maximizing response time and reducing stirring sensitivity (Revsbech, 1989). In comparison, optical O_2 sensors (i.e., optodes) have been applied more frequently since their introduction to aquatic EC (Chipman et al., 2012) because they have the advantage of not consuming O_2, making them less susceptible to stirring sensitivity as there is no net transport of O_2 to the sensor (Klimant et al., 1995). However, recent work has also suggested that optodes, like commonly used Clark-type sensors, may have a variable response time due to changes in the boundary layer thickness caused by wave motions or zero-crossing velocities that temporarily limit transport to the sensor, an effect that peaks at the frequency of the waves (Bittig et al., 2014; Reimers et al., 2016a). To prevent sensor bias, microfluidic sensor housings (pumping fluid from the measurement point to negate wave velocities) and rotating instrument designs (preventing biased sensor separation corrections due to waves or orthogonal currents) have been developed, but also complicate instrument engineering (Long et al., 2015a, 2019).

The issue of waves, which is unique to aquatic EC, has largely focused on the biogeochemical sensors, but wave bias in the turbulence measurements from acoustic sensors is also of major concern (Amador et al., 2020; Benilov & Filyushkin, 1970; Bricker & Monismith, 2007; Rosman & Gerbi, 2017; Scully

et al., 2016; Shaw & Trowbridge, 2001; Trowbridge, 1998). Wave-bias in the turbulent velocities used to calculate fluxes have been observed due to slight variations in instrument orientation, leading to some of the horizontal wave-associated velocities contaminating the vertical velocity (Bricker & Monismith, 2007; Long et al., 2015b; Reimers et al., 2016a; Scully et al., 2016; Trowbridge 1998; Trowbridge et al., 2018). This contamination of vertical velocity by waves is a problem when turbulence and surface waves are observed at similar or overlapping frequencies and requires multiple instruments (Shaw & Trowbridge, 2001; Trowbridge 1998) or wave-turbulence decomposition methods (Benilov & Filyushkin, 1970; Bricker & Monismith, 2007) to remove wave-bias. However, a careful consideration of site hydrodynamic conditions and instrument configurations can enable a process where the wave and turbulence frequencies do not significantly overlap, thereby allowing for the spectral separation of turbulence and waves (Long & Nicholson 2018; Scully et al., 2016) to remove wave-bias in chemical sensor and turbulence measurements caused by high-frequency surface waves.

Scully et al. (2016) describes and applies a procedure for removing wave bias in turbulence measurements in coastal settings, based on the frequency differences between turbulence and wave period (T_d). The Taylor frozen turbulence hypothesis relates wavenumber (k, in rad m^{-1}) to frequency (f, in Hz or cycles s^{-1}) based on the mean advection speed (U, in m s^{-1}), as:

$$k = \frac{2\pi f}{U} \tag{2}$$

Both atmospheric and oceanic measurements of momentum cospectra suggest that under unstratified conditions, the peak of the variance preserving cospectra occurs at $k \sim a/z$, where z is the height above the bottom where measurements are conducted and the constant a has been estimated to range from about 0.8 (Gerbi et al., 2008; Wyngaard & Coté, 1972) to 1.2–3.1 (Amador et al., 2020; Kirincich et al., 2010; Stacey et al., 1999). Therefore, as long as the frequencies associated with the dominant surface waves ($1/T_d$) are high and the mean advection speed is low, the majority of the turbulent fluctuations will be at frequencies lower than the surface waves when:

$$\frac{2\pi z}{UT_d} > a \tag{3}$$

For example, at common shallow water conditions where the values of T_d do not exceed 4 s and tidal currents are <0.2 m s^{-1}, this relationship is easily satisfied if measurements are conducted at $z = 0.50$ m away from the benthic surface (i.e., $[(2\pi z)/(UT_d) = 3.9]$), whereas a measurement height at $z = 0.05$ m away from the benthic surface would not (i.e., $[(2\pi z)/(UT_d) = 0.4]$). This method has been used to calculate turbulent fluxes by filtering out frequencies at and above the wave frequencies and has demonstrated that there is typically a clear spectral gap between the frequency of the dominant surface waves and the dominant frequencies of the turbulent flux when measurements are conducted at sufficient heights away from the interface boundary (Scully et al., 2016). While this process removes the majority of wave bias, it may also remove some high-frequency turbulent fluctuations, and some wave bias may still be present at lower frequencies due to the advection of turbulence by wave orbital velocities (Rosman & Gerbi, 2017).

This manuscript addresses a major issue that limits the application of boundary layer exchange techniques, specifically the aquatic EC technique, in shallow environments where waves are present. A primary objective of this highly interdisciplinary topic is to produce and communicate results that are easily discernable and translatable to the aquatic EC community. A review of existing aquatic EC literature is presented to highlight the predominance of EC applications in shallow water where waves are likely to be present, and the conditions and configurations of previous EC studies. A new analysis framework for flux calculation is presented, where the cross-power spectral density is accumulated from low frequencies, up to the wave frequencies, to calculate interface fluxes. This method effectively removes wave bias from both sensor and turbulence measurements, and specific guidelines are provided to ensure that this method can be applied, based on site hydrodynamics and instrument configurations. Also presented is the potential use of slow-response sensors using these same guidelines that will enable a wider range of sensors to be applied to the EC technique in the future.

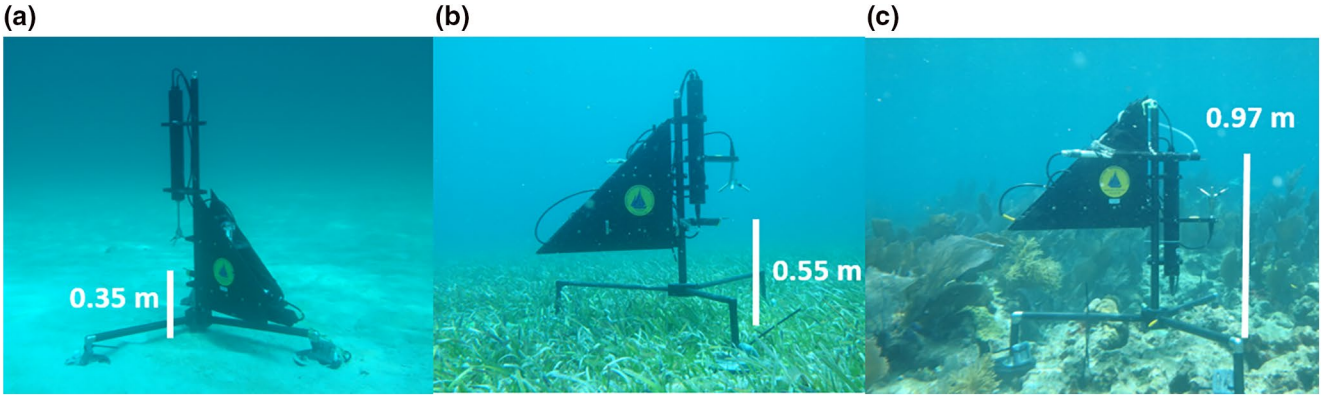

Figure 1. Eddy Covariance Hydrogen ion and Oxygen Exchange Systems (ECHOES) deployed at sand (a), seagrass (b), and reef (c) sites on or adjacent to Little Grecian Rocks Reef in the Florida Keys, Florida, USA. Measurement heights are indicated by white bars and text.

2. Methods

2.1. Literature Review

This research presents a review of the EC literature consisting of 62 field-based manuscripts published since the introduction of aquatic oxygen EC for biogeochemical investigations (Berg et al., 2003). These manuscripts were separated into different study sites defined by either, having different measurement heights or, different water depths. In manuscripts where a range of sites with different depths were analyzed, the smallest and greatest depths are reported. The depths, measurement heights, solutes, sensors, benthic roughness elements, wave parameters, environment, burst length, and Reynolds decomposition method were extracted from the manuscript text when reported. Cospectral frequencies and peak current velocities were taken directly from the text or visually estimated from figures. Measurement heights of the sensors were modified by subtracting biological canopy heights or physical barrier heights when reported.

2.2. Field Sites

The field sites were located ~7 km offshore of Key Largo, Florida, USA at the southern tip of Florida in the Florida Keys. The sites were located on or adjacent to Little Grecian Rocks Reef with a site on the reef crest (25.119016°N, -80.300504°W, Figure 1c) at 2.9 m mean depth, in a seagrass bed located ~225 m to the northwest of the reef site (25.120328°N, -80.302222°W, Figure 1b) at 4.8 m mean depth, and in a sandy site located ~300 m to the southwest of the reef site (25.117320°N, -80.303069°W, Figure 1a) at 6.3 m mean depth. The reef site is described in substantial detail (3-dimensional and species analyses) in Hopkinson et al. (2020), where the EC instrument can be seen near the center of the image analyses (in Figure 6 of Hopkinson et al., 2020) during its deployment in this study. This reef site is substantially degraded with its benthic surface and primary production dominated by octocorals, algae and rubble (Hopkinson et al., 2020; Owen et al., 2020). The seagrass site was dominated by dense *Thalassia testudinum* (turtlegrass) with a canopy height of 0.2 m underlain by carbonate sands. The sandy site was composed of carbonate sands with microalgal mats (Figure 1a) and migrating bedforms 0.1 m in height. Research was conducted from June 24 to June 29 in 2018 with the seagrass deployment beginning on the 24th and the sand and reef deployment beginning on the 25th of June, 2018.

2.3. Instrumentation

The EC systems used here, known as Eddy Covariance Hydrogen Ion and Oxygen Exchanged System (ECHOES, Long et al., 2015a) consisted of an Acoustic Doppler Velocimeter (ADV, Nortek) that was coupled to a FirestingO_2 Mini fiber-optic O_2 meter with a fast-response (~0.3 s) 430 μm diameter optode (Pyroscience) (Long et al., 2015a, 2019; Long & Nicholson, 2018) and a fast-response (~0.6 s, Figure S1)

Honeywell Durafet® III pH sensor with a preamp Cap Adapter and a custom isolation amplifier (based on Texas Instruments ISO124P). The ECHOES systems logged the three-dimensional velocity, depth, O_2 optode, pH sensor, and triaxial Inertial Measurement Unit (IMU, MicroStrain model 3DM-GX3) at a frequency of 16 Hz continuously. Using 6 rechargeable lithium ion batteries (50 Watt h, Nortek #220007) the system could operate continuously for ~4.5 days. All instrumentation was mounted to a light-weight, passively rotating carbon fiber frame (Figure 1). A bubble level affixed to the ADV mount allowed for precise leveling during field deployment by SCUBA divers. Stakes (sand and seagrass sites) or lead weights and zip ties (reef site) maintained instrument location and orientation. The measurement height, or location of the ADV measuring volume and sensors, above the sediment surface was determined by placing it at a height that was greater than twice the canopy (0.5 m reef canopy, 0.2 m seagrass canopy) or bedform (0.1 m) height (Figure 1) as recommended by terrestrial EC guidelines where twice the canopy height, and up to 5 times the canopy height in patchy environments, is recommended (Burba & Anderson, 2010; Long et al., 2015b).

The microfluidic flow-through sensor design has a small volume (0.33 cm^3) and a KNF Micropump (model NF10) with a flow rate (100 mL min^{-1}) that combine to have a quick flush rate (5 Hz) while protecting and preventing light interference for both O_2 and pH sensors. The microfluidic intake was located 0.025 m behind the ADV measuring volume (see Berg et al., 2015; Donis et al., 2015) to prevent disruption of ADV-measured flow rates (Long et al., 2015a). The microfluidic housing mounted tightly over the Durafet III sensor tip and has a small chamber for inserting the O_2 optode, that is located at the end of a 0.04 m long, 0.003 m inside diameter copper intake tube and filter, with the outlet of the microfluidic chamber connected to the pump intake (Figure S2). A passive flow meter (0–100 ml min^{-1}) connected to the pump outlet was used to confirm pumping rates during deployment.

A separate frame at each site contained an Odyssey (Dataflow Systems, New Zealand) photosynthetically active radiation (PAR) sensor and a Seabird SeapHOx (measuring salinity, temperature, depth, O_2, and pH). The SeapHOx was factory calibrated and the Odyssey PAR sensors were calibrated to a HR-4 spectroradiometer system (HOBI Labs HydroRAD-4) using the methods of Long et al. (2012b).

2.4. EC Analysis Framework

The 16 Hz data were averaged to 8 Hz for analysis. The ECHOES O_2 and pH sensors were calibrated to the slow-response SeapHOx sensors by least-squares regression. The pH was converted to H^+ ion concentration for all calculations. The ADV velocity data was removed from analysis when the beam correlation was <50%. The means for Reynolds decomposition were determined using a 5 min moving average window. The period over which the flux was determined, or burst length, was 15 min, with subsequent averaging to hourly rates. Rotations to East, North, and Up coordinates based on the IMU data were conducted (see Long & Nicholson 2018) followed by a planar rotation (see Lorke et al., 2013) for each instrument deployment.

Standard EC analysis was conducted to calculate $O_2\left(\overline{w'O_2'}\right)$, $H^+\left(\overline{w'H^{+'}}\right)$, and momentum $\left(\left(\overline{w'u'}\right)^2+\left(\overline{w'v'}\right)^2\right)^{1/2}$ fluxes (e.g., Equation 1) where u and v indicate the horizontal components of the velocity and w represents the vertical velocity. Cross Power Spectral Densities were also used to calculate O_2, H^+ and momentum fluxes and were determined with the Matlab function "CPSD" by:

$$\text{Flux} = \sum_{f1}^{f_2} P_{w'c'}(f)\,df \tag{4}$$

Where the $P_{w'c'}(f)$ represents the CPSD as a function of physical frequency in Hz, c'represents the fluctuation components of O_2, H^+, or horizontal velocities, and the summation of the CPSD from the burst length (f_1 =15 min) up to the sampling frequency (f_2 = 8 Hz) or cutoff frequency ($f_2 = F_c$) determines the flux. The removal of wave frequencies was conducted by accumulating the CPSD at frequencies below the

F_c, estimated by $1/(2T_d)$. The T_d was determined by finding the maximum of the momentum CPSD at the frequencies where the waves were expected for the study sites (e.g., 0.1 > Hz < 1). Power spectral densities were determined using the Matlab function "PWELCH." Both the PWELCH and CPSD analyses used the default window and overlap. Wave orbital velocities (σ_w) were estimated by:

$$\sigma_w = \left(\overline{\left(u' - \overline{u}\right)^2} + \overline{\left(v' - \overline{v}\right)^2} + \overline{\left(w' - \overline{w}\right)^2} \right)^{1/2} \quad (5)$$

where the prime indicates the instantaneous velocity and the overbars indicate averaging over each burst.

The direct EC flux calculation ($Flux = \overline{w'c'}$) is mathematically equivalent to the CPSD calculation (Flux $= \sum_{f1}^{f_2} P_{w'c'}(f)df$). Therefore, the full-spectrum flux methods (direct covariance and CPSD, where $f_2 = 8$ Hz in the latter) were first compared by linear regression to confirm this agreement, followed by regression with the CPSD accumulated only up to the cutoff frequency ($f_2 = F_c$). If wave bias was present, this second regression would result in reduced correlation coefficients and slopes as this wave bias would be removed when the CPSD was only accumulated up to the wave frequencies. The normalized root square mean error (NRSME) between the different computation methods was determined by calculating the square root of the square of the difference between flux methods, averaging this value across each deployment and scalar, and normalizing this to percent by dividing by the range of the fluxes. This normalization method was used as the net, or average of the biogeochemical fluxes, is close to zero and would result in erroneous results when dividing by near-zero values (see Table S2).

The CPSD fluxes accumulated up to the wave band [CPSD (<0.125 Hz)] were then further refined by the results of Rosman and Gerbi (2017) that found turbulent fluxes above the dominant wave frequencies were minimally affected by wave advection by two criteria; (1) a velocity ratio, where σ_w is less than twice the current speed by $\frac{\sigma_w}{U} < 2$, and (2) a length-scale ratio, where the wave orbital magnitude is smaller than the length scale of turbulent eddies by $\frac{\sigma_w k_0}{\omega_w} < 0.5$, where k_0 is the roll-off wavenumber in rad m^{-1} determined from the inflection point of the cospectra (estimated from the zero point of the second derivative of the cospectra) and ω_w is the wave peak in rad s^{-1}. Therefore, periods that did not adhere to $\frac{\sigma_w}{U} < 2$ or $\frac{\sigma_w k_0}{\omega_w} < 0.5$ were removed in the final CPSD (<0.125 Hz) fluxes.

The cospectra of the direct covariance and CPSD analysis were also compared to the two-parameter semi-theoretical Kaimal model (Kaimal et al., 1972) by:

$$Co^*_{wc}(k) = \overline{w'c'}^* \left(\frac{7}{3\pi} \sin \frac{3\pi}{7} \right) \frac{1 / k_0}{1 + \left(k / k_0\right)^{7/3}} \quad (6)$$

where k is the wavenumber determined by $k = \frac{2\pi f}{U}$ and the model cospectrum (Co^*_{wc}) is defined by two parameters: the total unbiased theoretical flux ($\overline{w'c'}^*$) and the roll-off wavenumber (k_0) (Kaimal et al., 1972; Kirincich et al, 2010). The model cospectra was fit to the observed cospectra using nonlinear least-square fitting at wavenumbers below the surfaces waves (e.g., $k = \frac{2\pi f}{U}$, where $f < 0.125$ Hz) to determine the unbiased $\overline{w'c'}^*$ and k_0. The resulting full-spectrum semi-theoretical flux estimate, unbiased by waves, was accumulated across all frequencies to produce a cumulative flux or Ogive curve. The Kaimal estimates were then compared to the cumulative CPSD and direct covariance fluxes to determine the potential loss in the turbulent flux. To examine all tracers on the same scale, the fluxes were normalized by the total unbiased semi-theoretical Kaimal estimates.

3. Results

3.1. Literature Review

A total of 62 aquatic field-based biogeochemical EC manuscripts were identified (see Supplemental Information), which, when separated to individual studies based on different water depths and measurement heights, resulted in 105 studies for the purposes of this analysis (excluding this study). The use of Clark-type O_2 microsensors dominated ($n = 90$ studies, starting from Berg et al., 2003) with O_2 optodes becoming more popular recently ($n = 20$, starting from Chipman et al., 2012). Other sensors applied to EC included temperature ($n = 5$), galvanic O_2 ($n = 2$), conductivity ($n = 1$), nitrate ($n = 1$), hydrogen sulfide ($n = 1$), and pH ($n = 1$).

Previous studies have deployed the EC technique at water depths ranging from 0.3 to 2,500 m, but the majority of these studies were conducted at depths of less than 10 m ($n = 53$, out of 83 studies reporting depth, Figure 2a). The mean peak current velocity of previous studies was 0.170 ± 0.216 m s^{-1}, with a median of 0.12 m s^{-1}, and a range of 0.015–1.8 m s^{-1} (Figure 2b). The mean measurement height of previous studies was 0.25 ± 0.18 m, with a median of 0.20 m, and a range of 0.04–0.80 m (Figure 2c). Measurement heights of ≤0.15 m above the bottom were used in 42 studies, out of 102 studies reporting measurement heights. Some studies reported physical or biological canopy roughness elements ($n = 27$), which were subtracted from the reported measurement heights, resulting in a corrected mean measurement height of 0.190 ± 0.183 m, a median of 0.15 m, and a range of −0.365 to 0.8 m.

A total of 33 studies reported the contributing turbulent frequencies of the fluxes, which displayed a decrease in frequency with increased measurement height (Figure 2d). Both the highest and lowest contributing frequencies show a negative slope with increasing measurement height, and a significant difference from a zero-slope line. Applying $[(2\pi z)/(UT_d) = a]$ to previous studies conducted at <10 m depth that report the presence of waves indicated that the mean of the conditions and instrument configurations may allow for the separation of turbulence and wave frequencies when sampling heights are >0.15 m (assuming $a \approx 1$, Table 1). However, more than half of these <10 m depth studies reporting wave conditions were conducted at measurement heights ≤0.15 m and these low measurement heights combined with mean study conditions suggest that a distinct separation between turbulent and wave frequencies may not have been possible (assuming $a \approx 1$, Table 1). The majority of studies ($n = 60$, out of 105) did not report wave conditions.

For conducting Reynolds decomposition, 55 manuscripts used linear detrending, 25 used a moving or running average window, 13 used a combination or other method, and 12 did not report a mean determination method. The burst length, or period over which fluxes are calculated, was most commonly 15 min ($n = 74$ manuscripts) followed by 10 min ($n = 9$), <10 min ($n = 8$), 30 min ($n = 4$), 20 min ($n = 1$), variable ($n = 1$) or not reported ($n = 12$). A range of different data and time-series corrections including; velocity de-spiking (e.g., Goring & Nikora, 2002), various coordinate rotations (Lorke et al., 2013; Reimers et al., 2012), sensor time-lag corrections (Berg et al., 2015; Donis et al., 2015), low-frequency wave corrections (Reimers et al., 2016b), storage correction (Long & Nicholson 2018; Lorrai et al., 2010; Rheuban et al., 2014a), nonsteady state condition bias (Holtappels et al., 2013), slow sensor response time correction (McGinnis et al., 2008), flux loss due to photosynthetic bubble production and ebullition to the atmosphere (Long et al., 2020), stirring sensitivity correction (Holtappels et al., 2015), and platform motion corrections (Long & Nicholson, 2018) have been described and applied, and are discussed elsewhere, as noted.

3.2. Field Data

The three ECHOES and associated instruments were deployed for 4–4.5 days at each site (sand 96 h, seagrass 108 h, and reef 96 h; Figure 3) with a total of 84 h of overlap where all 3 ECHOES were collecting data at the same time. In these relatively clear subtropical waters the ADV velocity beam correlation was used to remove time periods where the correlation was <50% which resulted in the removal of 35.4% (34 h), 0.1% (0.75 h), and 4.4% (4.25 h) of the data from the sand, seagrass, and reef sites, respectively (Table 2). The removal of CPSD (<0.125 Hz) fluxes, when waves may impact lower frequency turbulent fluxes as demonstrated by Rosman and Gerbi (2017), resulted in the removal of 4.4% (4.25 h), 12.5% (13.5 h), and 64.1%

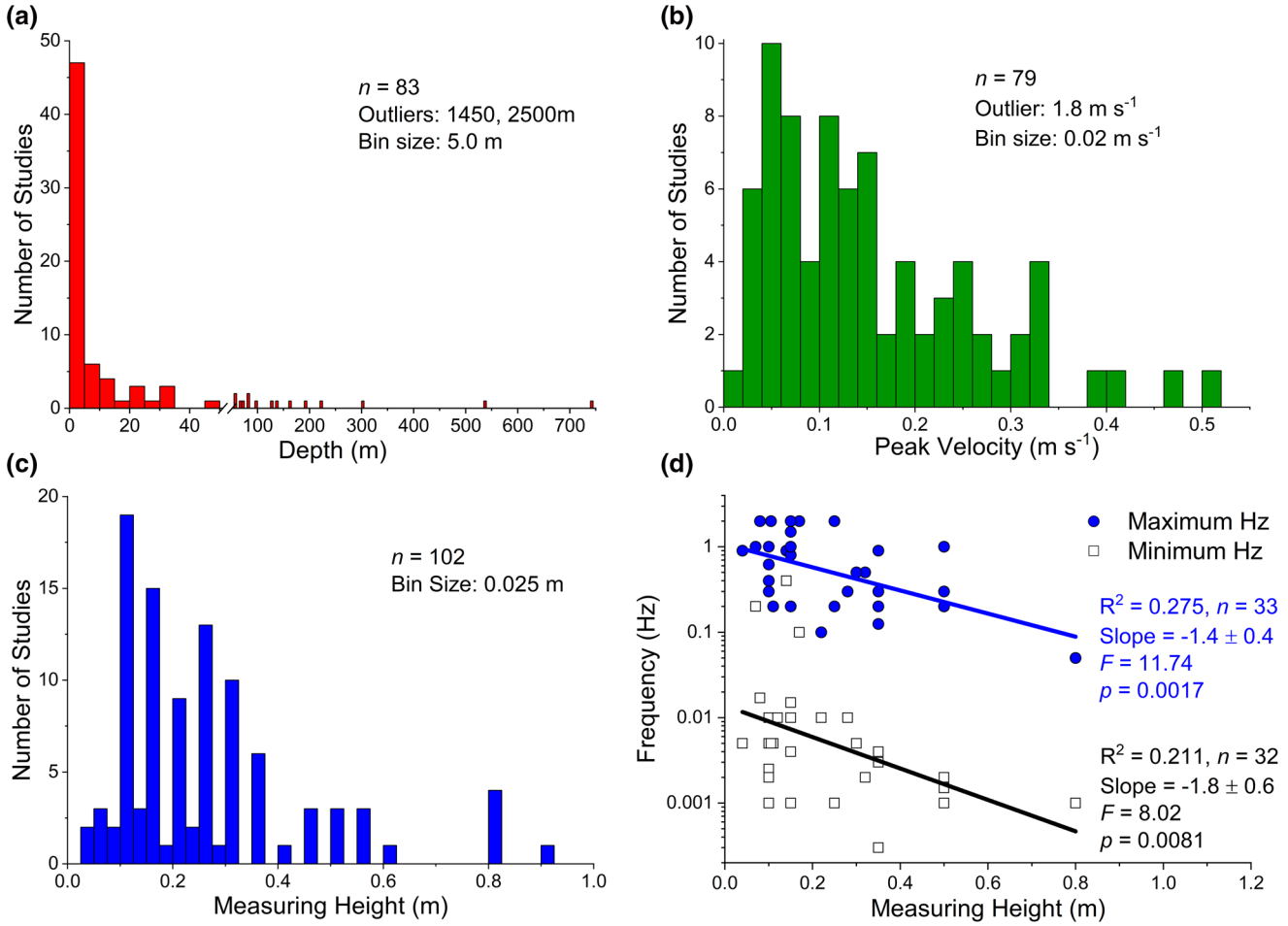

Figure 2. Histograms of the depth of biogeochemical eddy covariance studies (a) and the peak velocity measured in studies (b). Note the dominance of shallow-water studies where waves are likely present. Histograms of measurement heights (uncorrected for canopy or physical barrier heights) used in eddy covariance studies (c) and the associated frequencies of flux-carrying eddies which shift to longer scales with increasing measurement heights (d) where statistics represent a significant difference from a zero-slope line.

(61.5 h) of the data from the sand, seagrass, and reef sites, respectively (Table 2). At the reef site a substantial amount of pH data was also lost due to sporadic electrical issues that contaminated 72.4% (69.5 h) of the pH data. Fluxes showed expected diel trends with O_2 production and H^+ consumption during the day and

Table 1
Potential for a Spectral Gap Between Turbulence and Wave Frequencies in Different Studies Conducted at <10 m Depth

Site	Measurement height (z) m	Peak velocity (U) m s^{-1}	Wave period (T_d) s	$(2\pi z/(UT_d)$
*Previous studies (≤0.15 m z)	0.07 (−0.05 to 0.15, n = 17)	0.19 (0.02–0.5, n = 15)	2.8 (1–5, n = 6)	0.79
*Previous studies (>0.15 m z)	0.28 (0.0–0.8, n = 14)	0.11 (0.02–0.26, n = 13)	3.8 (3–4, n = 5)	4.26
This study—Sand	0.35 (0.1 m bedforms)	0.18	3.9	3.13
This Study—Grass	0.55 (0.2 m canopy)	0.12	4.1	3.19
This Study—Reef	0.97 (0.5 m canopy)	0.11	3.7	7.25

The * indicates previous studies that reported both the presence of waves and were conducted at <10 m depth are included. When biological canopy or physical barrier heights are reported, these have been subtracted from the reported measuring heights (see supplemental information). Numbers in parenthesis are the range and n from previous studies, or canopy and bedform heights (this study).

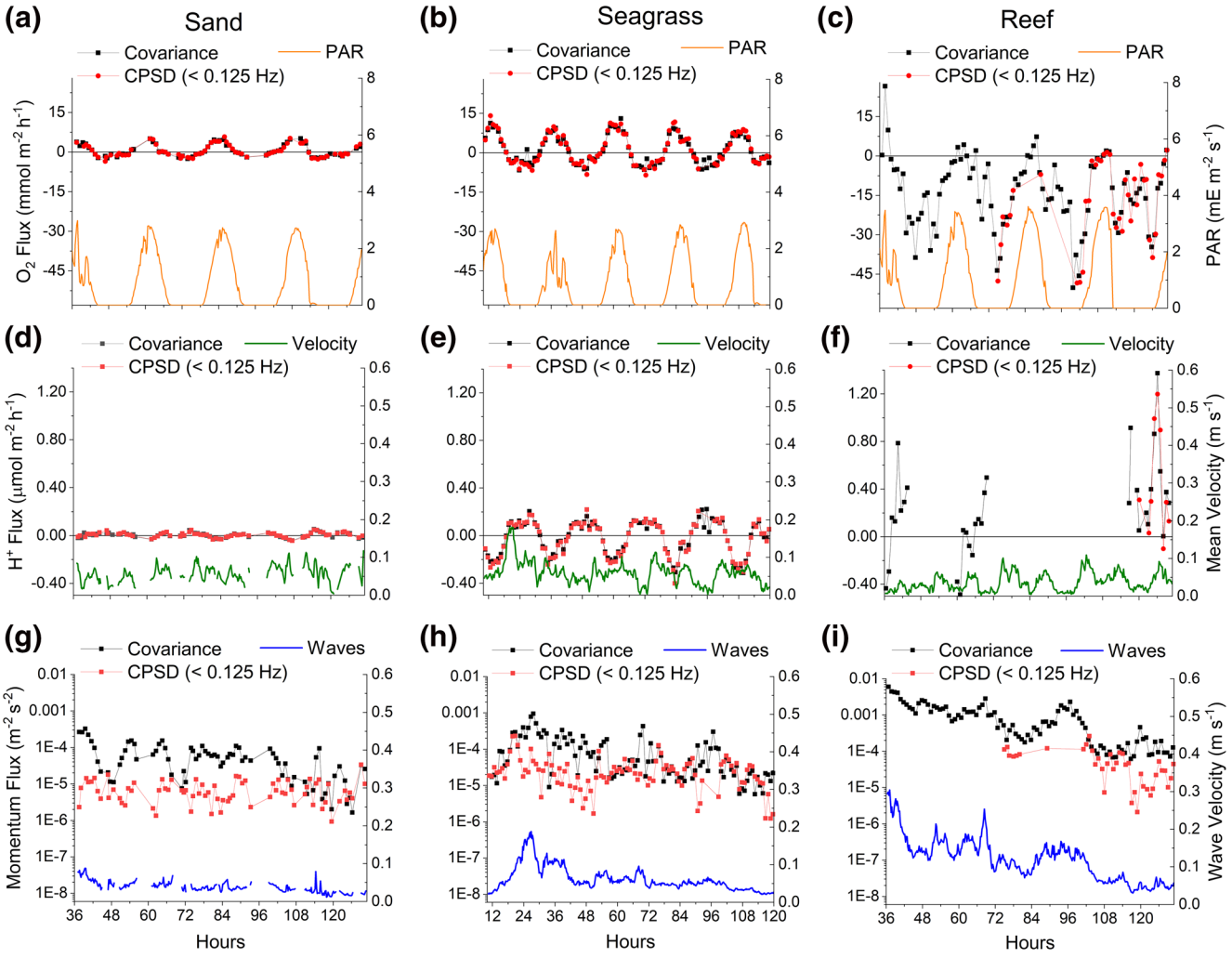

Figure 3. Time series data and fluxes at sand, grass, and reef sites beginning at noon (hour 12) on June 24, 2018. Oxygen (left a–c), H^+ (left d–f) and momentum (left g–i) fluxes determined by eddy covariance (black) and cross-power spectral densities accumulated below wave frequencies (<0.125 Hz, red). Time series of photosynthetically active radiation (PAR, orange); (a–c), mean velocities (green); (d–f) and wave velocities (blue); (g–i) are shown on the right axes.

O_2 consumption and H^+ production during the night (Figures 3a–3f). Biogeochemical fluxes were about an order of magnitude larger on the reef site compared to the sand site. Current velocities were dominated by diurnal tides and wave velocities generally decreased over the deployment period (Figures 3d–3i). Diel ranges of O_2 (171–237 µmol L^{-1}) and pH (8.06–8.17) were very similar between the adjacent sites.

Applying $[(2\pi z)/(UT_d) = a]$ to the study conditions suggests that there was a spectral gap between wave and turbulent frequencies (i.e., $[(2\pi z)/(UT_d) > 3.1]$, Table 1). Before applying this theory, the agreement between fluxes calculated using traditional direct covariance analysis (e.g., Equation 1) was compared to that of the Matlab CPSD function, accumulated across all frequencies. Across the sites (sand, grass, and reef) and scalars (O_2, H^+, momentum) the minimum R^2 was 0.92 with a maximum of 2.5 % normalized root square mean error (NRSME, Table 2, Figure 4). The lowest values were found for the scalar with the least data (n = 141 bursts, Reef H^+, Table 2) and the site with the second least data and smallest fluxes (n = 248 bursts, Sand H^+, Table 2, Figure 3d), respectively. The remaining majority of results had coefficients of determination of ≥ 0.99 and ≤ 1.0 % NRSME (Table 2) indicating the expected agreement between direct covariance and CPSD methods (Figure 4).

The wave period (T_d) at the sand, grass, and reef sites were 4.0 ± 0.5 (3.1–5.7 range), 3.9 ± 0.5 (2.6–5.2 range) and 3.7 ± 0.6 (2.0–5.3 range) s, respectively. By examining the power spectral density of the horizontal ve-

Table 2
Comparison of Direct Covariance, CPSD (All Hz), and CPSD (<0.125 Hz) Fluxes

			Covariance vs. CPSD (All Hz)			Covariance vs. CPSD (<0.125 Hz)		
Flux	Site	*n*	Slope (±SE)	R^2	NRSME (%)	Slope (±SE)	R^2	NRSME (%)
Oxygen	Sand	247	1.03 ± 0.01	0.990	1.0 ± 1.2	0.93 ± 0.02	0.935	3.0 ± 5.5
	Seagrass	430	1.02 ± 0.00	0.995	0.8 ± 0.9	0.89 ± 0.02	0.879	2.9 ± 8.1
	Reef	375	1.02 ± 0.01	0.994	0.7 ± 0.6	0.58 ± 0.03	0.539	4.1 ± 10.2
	Total	1,052	1.02 ± 0.00	0.996	0.3 ± 0.7	0.68 ± 0.02	0.666	1.8 ± 10.9
H^+	Sand	247	1.03 ± 0.02	0.915	2.5 ± 3.0	0.50 ± 0.04	0.409	7.0 ± 9.2
	Seagrass	430	1.02 ± 0.00	0.994	0.6 ± 0.9	0.94 ± 0.01	0.970	1.7 ± 2.1
	Reef	141	1.03 ± 0.02	0.963	1.4 ± 7.4	0.98 ± 0.03	0.911	1.7 ± 7.5
	Total	818	1.02 ± 0.01	0.937	0.2 ± 7.1	0.97 ± 0.01	0.914	0.5 ± 7.6
Momentum	Sand	247	1.00 ± 0.00	0.997	0.3 ± 1.0	0.03 ± 0.00	0.434	6.0 ± 21.5
	Seagrass	430	1.00 ± 0.00	0.999	0.2 ± 0.9	0.01 ± 0.01	0.001	5.7 ± 24.2
	Reef	375	1.00 ± 0.00	0.999	0.3 ± 0.7	0.04 ± 0.00	0.550	10.5 ± 21.0
	Total	1,052	1.00 ± 0.00	0.999	0.1 ± 0.7	0.04 ± 0.00	0.529	4.4 ± 23.3%

locity (e.g., Figures 5d–5f, S4d–S4f), especially during periods of high wave velocity and long wave periods, a cutoff frequency (F_c) of 0.125 Hz (8 s) was chosen as the frequency up to which the CPSD should be accumulated to remove wave bias (Figures 5 and S4). In all cases (scalars and sites) the coefficients of determination and slopes were reduced and the error increased indicating that the frequencies associated with the waves were contributing bias to the flux (Table 2). The maximum decrease in the slopes (50%) and highest NRSME (7.0 ± 9.2 %) was modest for the O_2 and H^+ fluxes compared to the substantial decrease in the slope (99%) and increase in NRSME and variance (10.5 ± 21.0) for the momentum fluxes (Table 2, Figure 4).

During periods of low-wave activity, the accumulated CPSD commonly exhibited a diminishing slope before the F_c under low wave conditions and spectral filtering had little impact on biogeochemical fluxes (Figures 5b–5c). This diminishing slope before the F_c was confirmed with the Kaimal semi-theoretical fits and suggested that the majority of the flux was being captured with the O_2, H^+, and momentum CPSD (<0.125 Hz) analyses, where only 3.8%, 3.4%, and 4.6 % NRSME, respectively, of the total unbiased semi-theoretical estimates were above the F_c (Figures 5a–5c). Deviations from the Kaimal fits were evident at higher frequencies, coinciding with wave frequencies, and were most apparent in the momentum fluxes with a 193.0 % NRSME (Figure 5), and were significant during wave-dominated conditions (Figure S4). Full-spectrum accumulation of the O_2 and H^+ CPSD calculated fluxes produced 4.8% and 9.1% NRSME compared to the total unbiased semi-theoretical Kaimal estimates (Figure 5) but had both positive and negative deviations from the semi-theoretical fits at wave frequencies (e.g., Figure 5a). Notably, the NRSME for the Kaimal nonlinear least-squares fits were 24.7%, 25.1%, and 32.2% for the O_2, H^+, and momentum fluxes, respectively.

In the majority of cases, the momentum flux exhibited significant bias at wave frequencies (Figures 4g–4i, 5a–5c, S4a–S4c). During conditions when the wave velocities were at least twice as high as the mean flow ($\frac{\sigma_w}{U} > 2$) there was substantial contributions to all of the fluxes at wave frequencies (i.e., Figure S4a–S4c), but these periods were removed by the criteria of Rosman and Gerbi (2017). Oxygen and H^+ power spectra (Figure 5) showed no variability at wave frequencies and only very limited variability due to waves in the rejected data (Figures S4e and S4f) while horizontal and vertical velocity spectra indicated significant power at wave frequencies (Figure 5). Furthermore, differences between sites and sampling heights (i.e., sand, 0.35 m sampling height, Figure 5d) indicated substantial power at wave frequencies predominantly in the horizontal spectra, where wave orbitals become compressed vertically when sampling closer to the bottom, while the reef (0.97 m sampling height) indicate a balance between power at wave frequencies in both the horizontal and vertical (Figure 5f). Across the sites, the absolute differences between the EC and CPSD (<0.125 Hz) fluxes (i.e., Figures 3a–3c) were positively correlated to the wave orbital velocity with

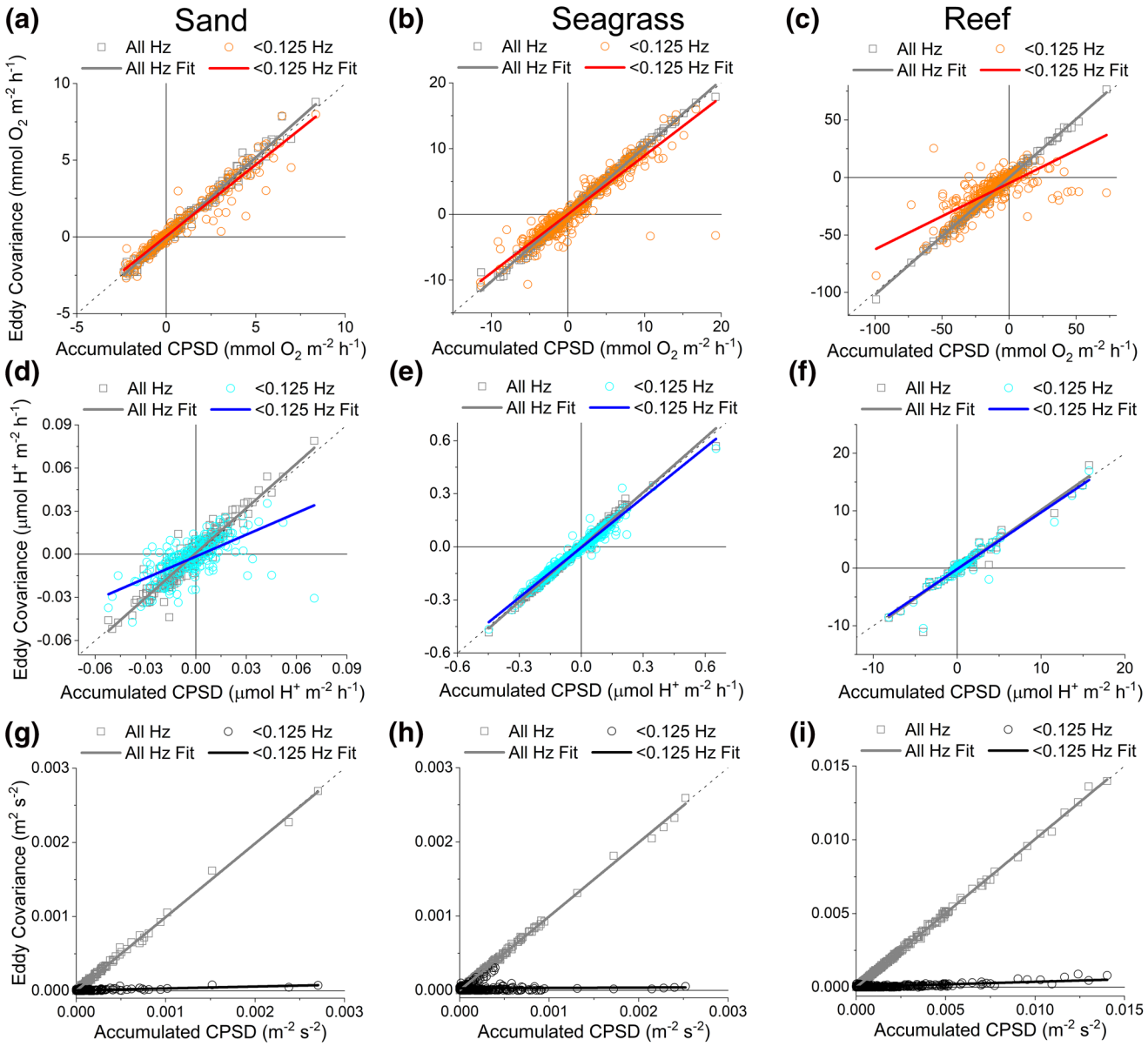

Figure 4. Comparison of fluxes determined from the cross-power spectral densities, accumulated across all frequencies, and fluxes determined from eddy covariance (gray boxes, gray lines, a–i) for the sand, grass, and reef sites. The comparison of fluxes determined from cross-power spectral densities, accumulated up to the wave frequency (<0.125 Hz), and fluxes determined from eddy covariance are shown for O_2 (orange circles and red lines, a–c), H^+ (cyan circles and blue lines, d–f), and momentum (black circles and black lines, g–i) fluxes. Each symbol represents an individual 15 min burst and all lines are linear regressions with statistics reported in Table 2.

slopes significantly different from zero and the strongest coefficient of determination for the momentum flux ($R^2 = 0.69$) followed by the O_2 flux ($R^2 = 0.22$), and H^+ flux ($R^2 = 0.08$) (Figure S3).

3.3. Ecosystem Fluxes

The hourly O_2 and H^+ CPSD (<0.125 Hz) fluxes across each deployment (Figures 3a–3f) were averaged by hour of day (Figures 7a and 7c) to enable the calculation of net daily fluxes averaged over the ~4 day deployments (Figures 7b and 7d). The method of calculation of net ecosystem metabolic (NEM) rates (e.g., Rheuban et al., 2014a) was chosen due to the significant data gaps in the sand O_2 and H^+ fluxes (Figure 3). Both sand and seagrass sites exhibited net positive O_2 fluxes and autotrophy (12.9 ± 4.0 and

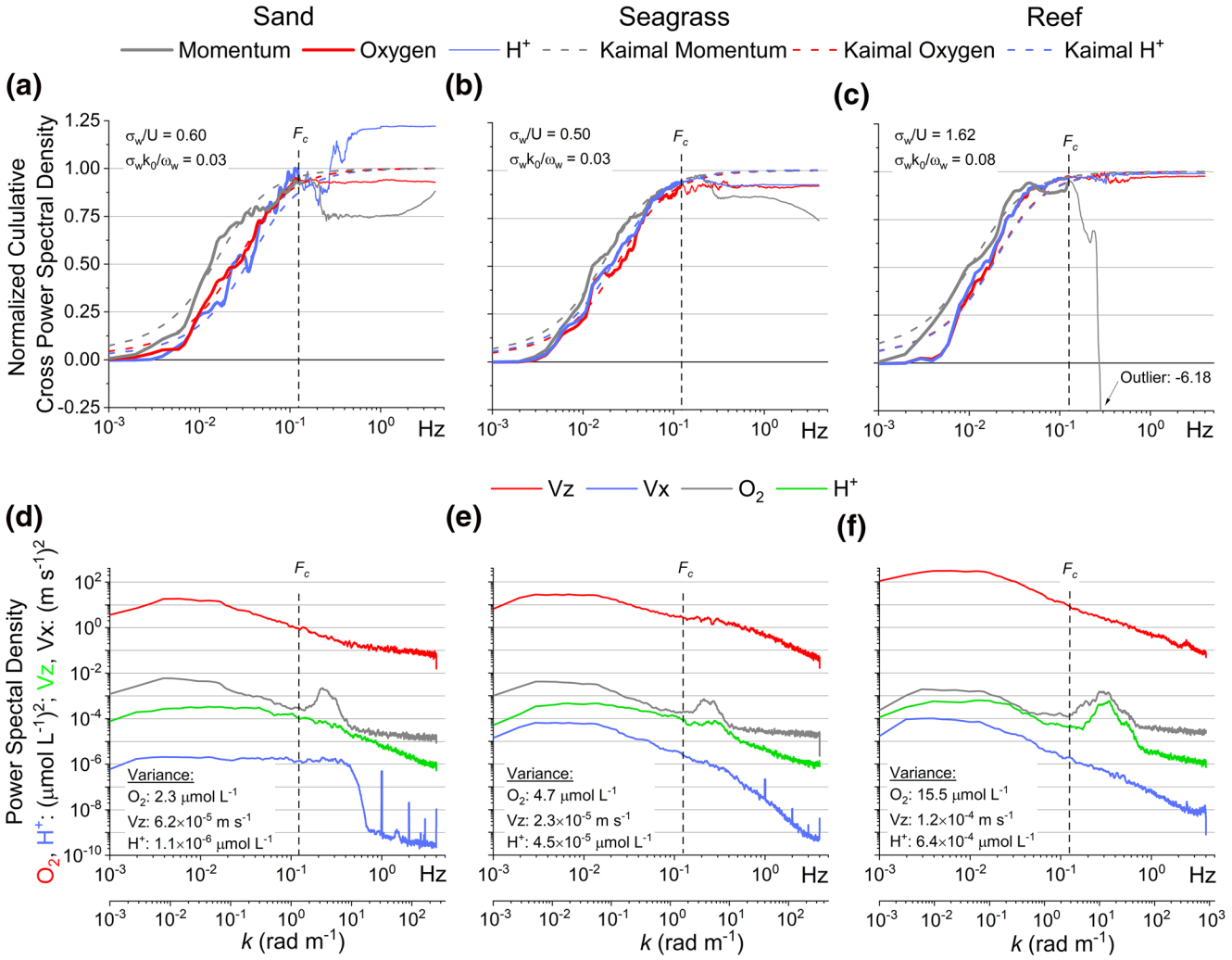

Figure 5. Spectral data from a low wave-energy period (hour 116, Figure 3). Normalized cumulative cross-power spectral densities show distinct differences between momentum fluxes and biogeochemical fluxes at wave frequencies. Kaimal semi-theoretical cumulative fluxes (dashed lines) were determined by fitting to the calculated cospectra below the F_c to estimate the full-spectrum unbiased semi-theoretical flux. Oxygen and H^+ spectra (lower panels, red and blue, respectively) show no variability at wave frequencies while horizontal (Vx, black) and vertical velocity (Vz, green) spectra indicate a significant power at wave frequencies. Furthermore, differences between sites and sampling heights (i.e., sand, 35 cm sampling height) indicate substantial power at wave frequencies in the horizontal spectra, where wave orbitals become compressed vertically when sampling closer to the bottom, while the reef (lower right, 97 cm sampling height) indicate a balance between power at wave frequencies in both the horizontal and vertical. The filtering criteria values of Rosman and Gerbi (2017) are shown as text (a–c). The variance of oxygen, vertical velocity, and H^+ (text, d–f) over each period indicate an increase in both biogeochemical tracer and vertical turbulence variances from the sand to reef sites.

23.0 ± 9.6 mmol O_2 m^{-2} d^{-1}, respectively) while the reef site had net negative O_2 fluxes and strong heterotrophy (−377.5 ± 50.2 mmol O_2 m^{-2} d^{-1}) (Figure 7b). The seagrass site had net negative H^+ fluxes indicating a consumption of acidity (−0.44 ± 0.28 μmol H^+ m^{-2} d^{-1}) and the sand site had near-balanced H^+ fluxes indicating no significant net production or consumption of acidity (0.08 ± 0.06 μmol H^+ m^{-2} d^{-1}) (Figure 7d). There was insufficient data to compute net daily fluxes of H^+ at the reef site.

4. Discussion

This research presents a new analysis framework and measurement requirements to enable biogeochemical EC measurements in the presence of waves. Since most studies using the EC technique have been conducted in shallow waters where waves are common, this has represented a significant setback for the small, but rapidly expanding biogeochemical EC community. Essentially, by measuring higher above the

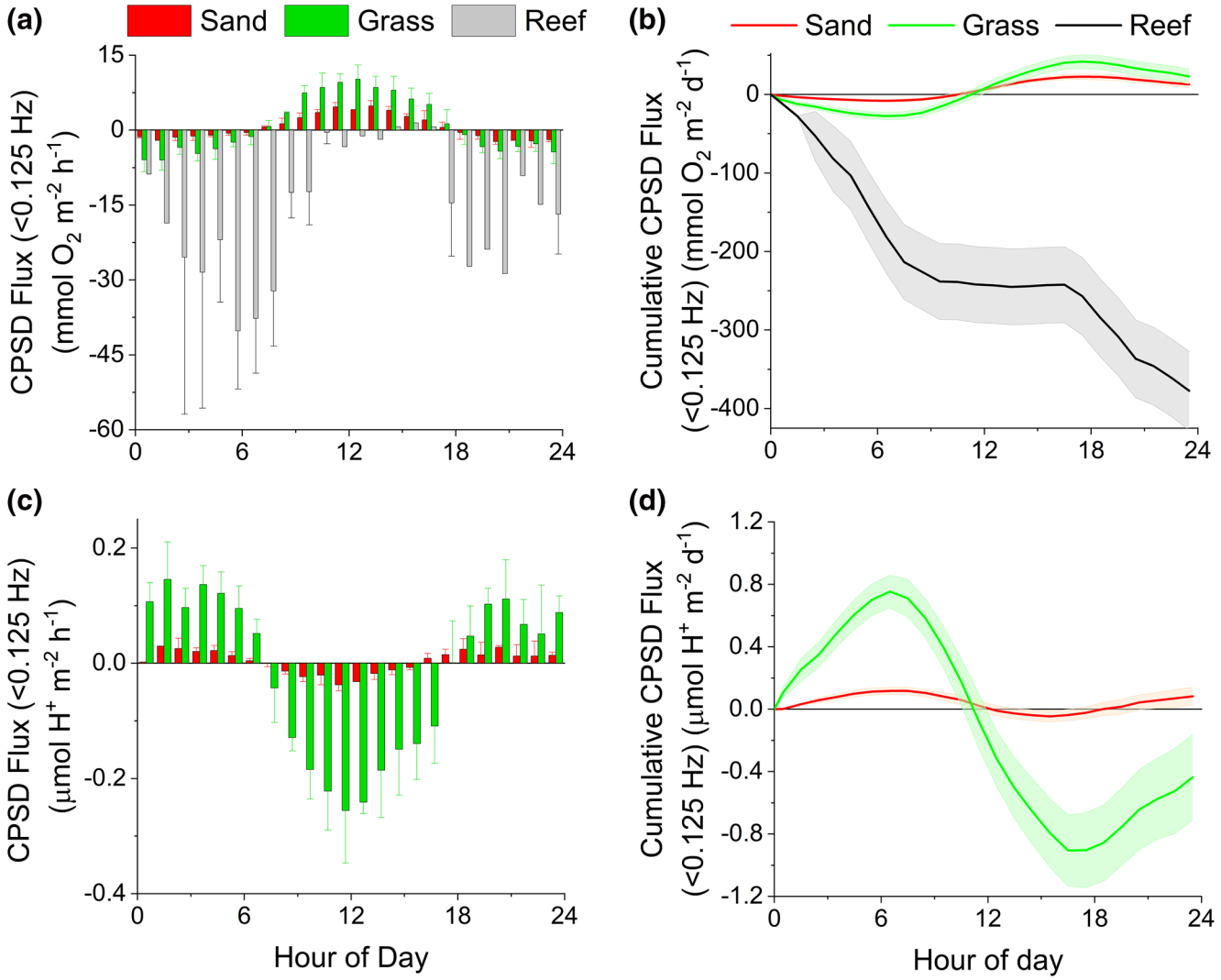

Figure 6. Accumulated cross power spectral density (<0.125 Hz) O_2 (a) and H^+ (c) fluxes averaged by hour of day from all data in Figures 3a–3f for sand (red), seagrass (green), and reef (gray) sites. The fluxes were accumulated across the hour of day, where shading indicates propagated error, to produce a net daily O_2 (b) and H^+ (d) fluxes for each site.

boundary than has been done traditionally (mostly < 0.25 m), the turbulent frequencies shift to longer scales, above the wave frequencies. The presented spectral analyses framework has been used to calculate turbulent fluxes by filtering out wave frequencies and has demonstrated that there is a clear spectral gap between the frequency of the dominant surface waves and the dominant frequencies of the turbulent flux when measurements are conducted at sufficient distance away from the interface at shallow water sites (Scully et al., 2016). Here, spectral analysis reveals conditions and measurement heights that produce gaps between turbulence and wave frequencies in both scalar (e.g., O_2 and H^+) and turbulence measurements. Therefore, waves can be spectrally filtered and effectively remove the majority of bias in both chemical sensor and turbulence measurements, which also allows for new EC chemical sensors that have slower response times to be applied to the EC technique.

4.1. Literature Review

The review of field-based biogeochemical EC studies revealed that the majority of studies have been conducted in shallow environments where waves are likely to occur. This potential for wave bias is compounded

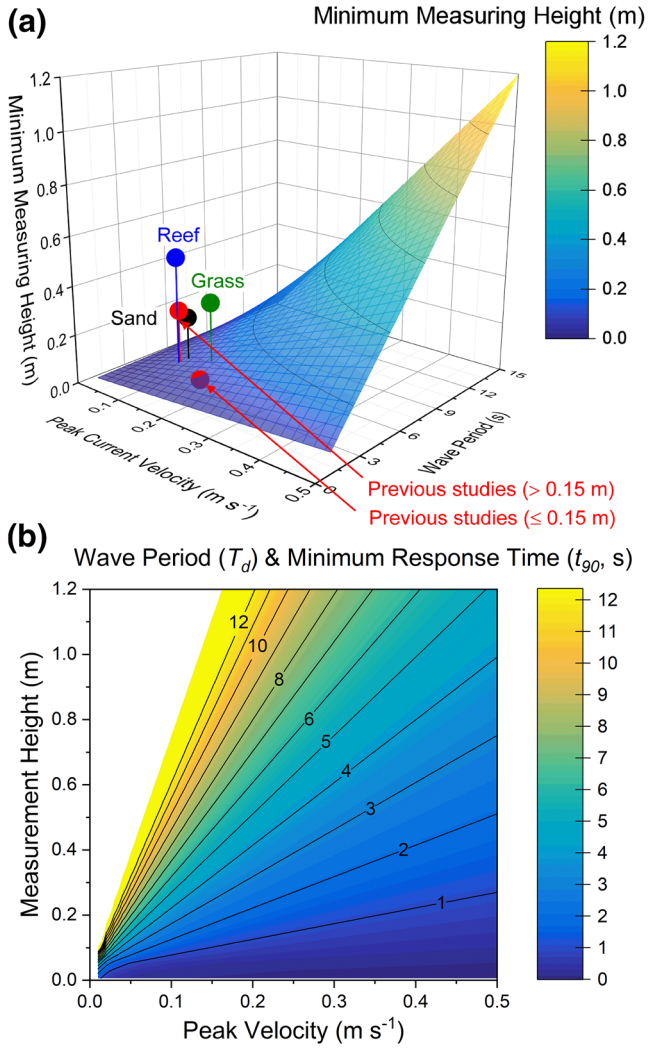

Figure 7. Minimum sampling heights that allow for a distinct gap between turbulence and waves frequencies based on $(2\pi z)/(UT_d) = 1$ (Equation 3, Scully et al., 2016) (a). Individual points show sampling heights over sand, grass, and reef sites (blue, green, and black dots) in this study minus the characteristic roughness heights of 0.1 (bedforms), 0.2 (seagrass canopy), and 0.5 m (reef canopy), respectively (Table 1). The Previous Studies represents the average measurement heights, T_d, and peak current velocities from previous studies conducted at <10 m depth, with measurement heights > 0.15 m, and waves; and those conducted at <10 m depth, with measurement heights >0.15 m, and waves (red dots, Table 1). Rearranging the equation $(2\pi z)/(UT_d) = 3.1$ (the minimum value of a demonstrated in this study and supported by the conservative upper estimates of Stacey et al. (1999), Kirincich et al. (2010), and Amador et al. (2020) to allow for separation of turbulence and wave frequencies) to solve for T_d and color shading by the assumption that the minimum response time is approximately the T_d (or the Nyquist frequency (2x) of the cutoff frequency $[F_c \approx 1/(2T_d)]$), produces a recommended minimum response time (t_{90}), (b) based on site conditions.

by the fact that the majority of studies (85%) used Clark-type microsensors, that have known biases created by wave-associated velocities and frequencies (Berg et al., 2015; Donis et al., 2015; Holtappels et al., 2015; Reimers et al., 2016a). Of the studies that reported the presence of waves and were conducted in shallow water, it was apparent that some studies sampled too close to the boundary (e.g., ≤ 0.15 m) to exhibit a clear separation between wave and turbulence frequencies, as described by $(2\pi z)/(UT_d)$ and illustrated by the color-mapped surface in Figure 7a. However, it is apparent that some previous studies could benefit from the presented spectral analysis framework, and that using higher measurement heights will benefit future studies, when waves are present (e.g., Figure 7b).

4.2. CPSD Analyses Framework

The presented CPSD analysis framework begins with a careful consideration of the site conditions, which inform appropriate measurement heights to allow for the spectral separation of turbulence and waves. When data is collected at appropriate measurement heights, the data can then be analyzed in the frequency domain, where the CPSD can be used to determine fluxes and wave periods can be evaluated. This spectral analyses can then be used to remove wave frequencies, by accumulating the CPSD up to the wave frequencies, effectively removing sensor and turbulence wave biases. Accumulating the CPSD across all frequencies can be used to compare with standard EC analyses, as well as determining the contribution to fluxes at wave frequencies. While this method is mostly applicable to shallow sites with high frequency surface waves and moderate current velocities, it is noted that these are the predominant conditions for most biogeochemical EC studies to date.

The presented CPSD method, when accumulated across all frequencies, produced an expected agreement with direct EC analysis with slopes of 1.0, $R^2 \geq 0.92$, and error ≤ 2.5%, where the lowest R^2 and highest error were found for H^+ fluxes with the smallest magnitudes at the sand site. These small discrepancies between the full-frequency CPSD and the standard EC analyses (Table 2) was likely due to the combination of the Hamming windowing function used in the CPSD calculation and the CPSD segmentation that by default splits the times series into eight segments to conduct the fast Fourier transform, while the direct EC analyses were conducted on the continuous time series data. When the CPSD was accumulated only up to the wave frequencies (i.e., the cutoff frequency, F_c) there was a decrease in the flux in all cases, with a substantial decrease in the momentum flux, followed by less pronounced decreases for the biogeochemical tracers of O_2 and H^+. The large decrease in the momentum flux is expected as waves bias both horizontal and vertical velocities that are used to calculated the momentum flux, while O_2 and H^+ sensors are not affected at wave frequencies as they are located in a microfluidic housing that removes wave velocities by placing the sensors in a constant-flow environment. However, wave bias is still present during high-wave periods due to the vertical velocities used to calculate the biogeochemical fluxes, albeit much lower than the momentum fluxes that includes both horizontal and vertical wave components.

The NRSME for biogeochemical (≤7.0%) and momentum (≤10.5%) fluxes was used to estimate potential errors due to waves, as diminishingly small fluxes (e.g., early morning and evening O_2 fluxes near zero)

can lead to very large RSME estimates (e.g., 315%, Table S2) when dividing by near-zero fluxes during crepuscular periods. These large RSME (37%–315%, Table S2) are comparable to individual maximum flux errors reported for sensor separations (67%; Berg et al., 2015), analog to digital resolution (64%; McGinnis et al., 2011), coordinate rotations with low-frequency waves (±50%; Reimers et al., 2012), nonsteady state conditions (100%; Holtappels et al., 2013), stirring-sensitivity (100%, Holtappels et al., 2015), low-frequency waves, stirring sensitivity and sensor separation (150%; Reimers et al., 2016a), and motion corrections for moving platforms (200%, Long & Nicholson 2018). In comparison, the NRSME are more consistent with studies that report average error estimates for slow response times (5%–10%; Lorrai et al., 2010; McGinnis et al., 2011; Chipman et al., 2012), stirring sensitivity (<15%; Attard et al., 2014, 2015, 2018; Volaric et al., 2018), spatial variability of footprints (<5%; Attard et al., 2015), and storage corrections (<10%, Plew 2019). Thus, the NRSME estimates provide better error comparisons between studies as the errors are not inflated by diminishingly small values and errors are normalized by the flux range, which has been determined to vary by at least four orders of magnitude from deep sea (Berg et al., 2009) to coral reef (Long et al., 2013) ecosystems.

The fluxes generally exhibited a diminishing slope before reaching the F_c, demonstrating the relationship described by $(2\pi z)/(UT_d)$, where there is a distinct spectral gap between the turbulence and wave frequencies. This was supported by the Kaimal semi-theoretical model estimates, where only about 4% of the semi-theoretical flux was estimated to be above the F_c (Figure 5) which was substantially lower than the error of the Kaimal nonlinear least-squares fits themselves (≥25%). In comparison, the full spectrum accumulation of the CPSD fluxes led to errors of about 5%–200%, which was most evident in the momentum flux, and biogeochemical fluxes had both positive and negative deviations from the semi-theoretical fits at wave frequencies (e.g., Figure 5a)

During extreme wave conditions at the reef site, where current velocity was 10-fold lower than wave velocities, fits to the Kaimal model often differed between the three tracers, did not clearly exhibit a diminishing slope before the F_c, and the calculated flux estimates differed substantially from the Kaimal model estimates (e.g., Figure S4). However, these data were rejected by the criteria developed by Rosman and Gerbi (2017) that determined that during low flow and high wave orbital velocities the low-frequency part of the cospectrum is impacted by wave advection of turbulence. It is important to note that shallow-water, high-roughness environments, such as shallow reefs, are a very challenging location to determine turbulent fluxes (Davis et al., 2020). However, the high magnitude of biogeochemical activity in shallow waters (i.e., large vertical gradients) makes biogeochemical flux measurements feasible during some hydrodynamic conditions, especially when compared to momentum fluxes.

While the Kaimal semi-theoretical model was useful for examining spectral shape and estimating the total unbiased theoretical flux, it should be applied carefully to biogeochemical fluxes because the nonlinear least-squares fits did not converge when fluxes were very small or close to zero during crepuscular periods (e.g., changes in the sign of the flux at dusk and dawn). Momentum fluxes generally did not suffer from this issue as diminishingly small fluxes were removed by the filtering criteria (e.g., Rosman & Gerbi, 2017) or were removed due to low beam correlations (e.g., < 50%). In comparison, the analogous near-zero biogeochemical fluxes were not removed by any filtering criteria, but rather were of significant interest as these periods indicate a balance between biogeochemical processes (e.g., production and respiration; acid consumption and production) that occurred on a diel cycle. While the Kaimal model was difficult to validate across all biogeochemical fluxes, the use of Kaimal model estimates in combination with momentum fluxes are very useful for describing processes and theory (e.g., the large wave bias in the momentum cospectra and fluxes that were not always apparent in the biogeochemical cospectra and fluxes, Figure 5). Therefore, the examination of both physical (e.g., momentum) and biogeochemical (e.g., O_2 and H^+) cospectra and fluxes concurrently is highly advantageous to explain biogeochemical processes and validate the flux determination methods.

In a previous study by this author, Long et al. (2015c), the presented cumulative cospectrum (Figure 8 in Long et al 2015c) illustrate an ideal application of the presented CPSD methodology, as there is a distinct separation between the turbulence and wave frequencies. In this example, the measurement height was 0.175 m (0.35 m measurement height - 0.175 m seagrass canopy height), flow velocities were very low (0.011 m s^{-1}) and wave periods were very fast (~1.4 s) (Long et al., 2015c). Applying these parameters to

$(2\pi z)/(UT_d)$ results in a value of 71.4, suggesting a substantial gap between turbulence and wave frequencies, which is apparent in the cumulative cospectrum that indicate a diminishingly small slope from 0.1 Hz up to the wave frequencies (~0.5–1 Hz).

In another EC study, by Kuwae et al. (2006), where current velocities from ~0.1 to 0.2 m s^{-1}, wave periods of 1–4 s, and measurement heights of 0.07–0.17 m produced values of $(2\pi z)/(UT_d)$ of 0.6–10.7, suggesting that the CPSD method could also be applied to their study site during some periods. Kuwae et al. (2006) shows cumulative spectra and cospectra that (1) illustrate wave-biased vertical velocity spectrum with no effect in O_2 spectrum, (2) a typical turbulence-dominated cumulative cospectrum with frequencies from 0.01 to a diminishing slope at 0.2 Hz and a negative contribution at 1–2 Hz, and (3) cumulative cospectra that indicate significant contributions at wave frequencies from 0.2 to 1 Hz. These examples from Kuwae et al. (2006) are similar to the full-frequency spectra and cospectra presented in this study, notably for (1) Figure 5, (2) Figures S4a–S4c, and (3) Figure S4c.

These previous studies (Kuwae et al., 2006; Long et al., 2015c) were both conducted with Clark-type microsensors which have been shown to be biased by wave orbital velocities (Berg et al., 2015; Donis et al., 2015; Holtappels et al., 2015; Reimers et al., 2016a) but these previous studies also suggest that wave velocities may cause scalar transport through the advection of porewater (Kuwae et al., 2006) or advection of turbulent motions or scalar variances through a fixed measurement point (Gerbi et al., 2008; Long et al., 2015c; Lumley & Terray, 1983; Rosman & Gerbi, 2017). Whether these wave-frequency variations are due to sensor biases (e.g., Holtappels et al., 2015; Reimers et al., 2016a), instrument orientation or tilt biases (e.g., Bricker & Monismith, 2007; Scully et al., 2016; Trowbridge 1998), or are actual transport or advection at wave frequencies (Gerbi et al., 2008; Kuwae et al., 2006; Lumley & Terray, 1983), the presented CPSD method, in combination with appropriate measurement heights, provides a specific framework to separate turbulent and wave-associated fluxes to overcome these biases, or to quantify fluxes associated with wave frequencies.

4.3. Sensors and Waves

The spectra for O_2 and H^+ show very limited variability associated with the wave peaks present in the vertical and horizontal velocity spectra, even during extreme wave conditions at the reef site. This suggests that the microfluidic sensor housing effectively removed wave bias from the sensors (Long & Nicholson, 2018) and/or that increased measurement heights decreased the vertical gradient to the point that advection by waves is not detectable by the resolution of the O_2 and H^+ sensors. The active pumping past the sensors created a constant-flow environment negating zero-crossing velocities and removed any concerns related to the sensor boundary layer and associated sensor response times (see Reimers et al., 2016a). These optical O_2 and H^+ ion selective field effect transistors (ISFET) sensors are sensitive to light interference (Long et al., 2015a) and therefore benefited from the darkened housing, although light interference for the O_2 optode only occurs in very shallow water due to its use of red light that is quickly attenuated with water depth. The rotating base allowed the precise correction for the separation between the sensors (Donis et al., 2015; Holtappels et al., 2015; Reimers et al., 2016a) using the known sensor separation, flow rate and the fact that that sensors were always oriented in line with the flow (Long et al., 2019). The Inertial Measurement Unit (IMU, housing a triaxial accelerometer, gyroscope, and magnetometer) measured the exact instrument orientation, movement and acceleration to allow for coordinate matrix transformation to account for platform rotation and movement (Long & Nicholson 2018). This new instrument design and motion correction is based on similar advancements used in atmospheric ship or buoy-based EC measurements to correct for platform motion (e.g., Edson et al., 1998; Flügge et al., 2016; McGillis et al., 2001).

This ECHOES measurement system including microfluidics (Long et al., 2015a) and IMU integration (Long & Nicholson 2018) represents a significant advancement of the EC technique that allow it to overcome previous challenges related to sensor wave bias and sensor separation corrections (Berg et al., 2015; Donis et al., 2015; Holtappels et al., 2015; Reimers et al., 2016b). However, while this ECHOES instrument design removed concerns related to sensor wave bias, it also complicated instrument engineering, had additional power requirements due to the use of a pump, and may not effectively rotate at very low current velocities. Importantly, this instrument configuration cannot remove bias in the vertical velocities used to calculate the flux. Thus, the presented combination of methodological improvements and the CPSD analysis framework

is preferable to effectively remove wave bias from EC flux measurements. However, future studies applying O_2 optodes, O_2 Clark-type microsensors, or other sensors in a traditional, fixed, open-sensor EC instrument (e.g., Berg et al., 2003) will still benefit substantially from the CPSD analysis framework by removing wave bias caused by sensor sensitivity to wave velocities as well as removing wave frequencies that can cause bias in sensor separations corrections.

This manuscript presents the first use of a Honeywell Durafet® III pH sensor in an EC instrument. The reduction of noise in the signal was a major initial challenge with good results produced by using an optically coupled power supply and amplifier. However, it was still apparent that there was low density in the power spectra across frequencies, especially at the sand site. This was exhibited in the fairly flat power spectal density and low variance for the sand site (Figure 5d) and may indicate a lower threshold for resolving the H^+ flux (sand site, $\pm$ 0.03 μmol m^{-2} h^{-1}), whereas fluxes were about an order of magnitude larger at the seagrass and reef sites. This lower resolution for the H^+ data was also apparent in the highest error and lowest coefficients of determination when comparing the full-spectrum CPSD and EC flux calculation methods. The notable roll-off of the H^+ spectra at the sand site, and to a lesser extent at the seagrass site, occurs at about half of the wave frequency (consistent with the minimum and maximum pressure of a passing wave) and may indicate the known pressure sensitivity of Durafet sensors due to mechanical strain (Martz et al., 2010), but this requires further investigation. However, the use of H^+ ISFET sensors (along with O_2 sensors) is promising as a biogeochemical tracer due to its ability to be used in carbonate chemistry models to determine rates of calcification and dissolution (Long et al., 2015a; Takeshita et al., 2016).

4.4. Ecosystem Fluxes

The determined fluxes across the sites showed expected diel trends with generally positive O_2 fluxes during the daytime and negative O_2 fluxes at night. The H^+ fluxes showed the opposite diel trend, consistent with CO_2 consumption by photosynthesis during the day and CO_2 production by respiration at night. Both seagrass and sand O_2 fluxes exhibited net autotrophy, but the reef site showed strong heterotrophy likely due to the predominance of octocorals, algae, and rubble at this heavily degraded reef site (Hopkinson et al., 2020, Owen et al., 2020). Both the seagrass and sand O_2 fluxes are consistent with previous measurements nearby in a similar depth seagrass meadow by Long et al. (2015b) (NEM = 37 ± 31 mmol O_2 m^{-2} d^{-1}) and in a slightly deeper sandy site by Berg et al. (2016) (flux range = −2 to 4 mmol O_2 m^{-2} h^{-1}). The study sites were visited frequently during the afternoon, when high irradiance and high O_2 saturation sometimes cause bubbles to form on photosynthetic organisms, but the production of bubbles was not observed at these sites. However, I cannot conclusively determine that bubble ebullition of O_2 did not bias the presented O_2 fluxes (see Long et al., 2020).

Notably, the reef net heterotrophy found here is a shift from the net autotrophy or balanced metabolism found nearby at Grecian Rocks Reef in 2009–2010 (Long et al., 2013) and may reflect differences between sites, the continuing degradation of the northern Florida Keys Reef tract (Muehllehner et al., 2016), and particularly to the proliferation of a bloom of red algae (*Galaxaura* spp.) following Hurricane Irma in 2017 that persisted through the time of our measurements in 2018 (Hopkinson et al., 2020, Owen et al., 2020). The H^+ fluxes observed at our sand site (±0.03 μmol m^{-2} h^{-1}) are about an order of magnitude lower than those found at other biogenic calcium carbonate sandy sites (±0.4 μmol m^{-2} h^{-1}, Cyronak et al., 2013) but these previous data were obtained in an isolated lagoon with large diel pH changes from about 7.8-8.4 that drove changes in dissolution and calcification (Cyronak et al., 2013; Santos et al., 2011) compared to the much lower diel pH (8.06–8.17) at our sand site. The large H^+ fluxes found at this isolated lagoon (±0.4 μmol m^{-2} h^{-1}, Cyronak et al., 2013; −1.1 to 0.3 μmol m^{-2} h^{-1}, Santos et al., 2011) are more consistent with the magnitude of fluxes that were observed at our reef site (−0.5 to 1.1 μmol m^{-2} h^{-1}). The seagrass site was the only site that acted as a net acidity sink, consistent with studies that indicate seagrass meadows act as a carbon sink (e.g., Duarte et al., 2010).

4.5. Guidelines for Measurement Height and Sensor Response Time

In this study, the ADV and sensor measurement height above the sediment surface was determined by placing it at a height that was greater than twice the biological canopy or bedform height (Figure 1, Attard

et al., 2014; Long et al., 2015c) as recommended by terrestrial EC guidelines where twice the canopy height, and up to 5 times the canopy height in patchy environments, is recommended (Burba & Anderson, 2010). The resulting values for $[(2\pi z)/(UT_d)]$ ranged from 3.1 to 7.3 based on the site conditions, and it was evident that being at the upper range of previous estimates (e.g., $(2\pi z)/(UT_d) \approx 3.0$; Amador et al., 2020; Kirincich et al., 2010; Stacey et al., 1999) is beneficial to highlight and resolve the diminishing slope of the cospectra prior to the wave frequencies (Figure 5; Long et al., 2015c). Further, it is apparent that some studies sampled too close to the bottom to allow for spectral turbulence and wave separation as the mean of studies sampling <0.15 m from the boundary (and in < 10 m of water where waves were present) fall below the surface defined by $(2\pi z)/(UT_d) = 1$ (Scully et al., 2016), the minimum recommended measurement height (Figure 7a). Biological canopy heights (e.g., reef structures, macrophyte canopies) and physical roughness elements (e.g., grain size, and bedforms) should also be considered when choosing measurement heights, as measurement heights are commonly reported from the benthic surface, not the surface of biological canopies that, in some cases, also vary in height with current velocity when the canopy is flexible (i.e., seagrasses, Nepf, 2012).

With the recommended measurement heights, based on current velocities and wave period, it follows that if the frequency response of a sensor is ≥ the wave frequency, then the majority of the flux can be captured, potentially allowing for the use of lower frequency response sensors. This sensor frequency response is typically referred to as the sensor response time (t_{90}), which is defined as the time to reach 90% of the total signal change (e.g., 0.5 s or 2 Hz). The Nyquist frequency can be defined as the frequency required to capture a signal, and is defined as twice as large as the highest frequency of interest. Here, the highest frequency of interest to resolve is the F_c, so, the Nyquist frequency is $2\times F_c$, which is also the wave frequency and the required minimum sensor frequency response (e.g., $[2\times F_c \approx T_d \approx t_{90}]$). Therefore, rearranging the equation $(2\pi z)/(UT_d) = 3.1$ (or the conservative minimum value demonstrated in this study to allow for separation of turbulence and wave frequencies) to solve for T_d and color shading the surface defined by this relationship in Figure 7b, produces a recommended minimum response time (t_{90}) based on site conditions (Figure 7b). For example, at a common shallow-water site where current velocity is ≤ 0.2 m s^{-1}, T_d is ≤ 4 s, and measurements are conducted 0.5 m from the top of the bottom roughness elements, a sensor with a t_{90} of ∼ 5 s (0.2 Hz) can record all of the contributions to the CPSD flux accumulated up to the F_c. In cases where a slow response sensor is applied, the momentum flux and Kaimal models can be useful for evaluating whether the entire flux is being captured. However, if the frequencies above the F_c are of interest due to potential advection of turbulence or porewater at wave frequencies (e.g., Gerbi et al., 2008; Kuwae et al., 2006; Lumley & Terray, 1983), then a sensor that has a response equivalent to twice the wave frequencies would be required. This role of physical transport at wave frequencies remains unresolved and requires further study, but is largely outside the main objectives of biogeochemical EC studies where chemical and turbulence sensor wave-bias is a major impediment.

There are additional factors to consider when sampling higher above the bottom. Sufficient sensor resolution is required as vertical gradients decrease with increasing measurement heights. The magnitude of the flux, which is proportional to the vertical gradient, should also be taken into account (e.g., the order of magnitude difference between the sand and reef fluxes, along with their different measuring heights). Bias in the flux due to storage within the water column increases with height, and storage corrections are now commonly included with large measurement heights (Berger et al., 2020; Koopmans et al, 2020; Long et al., 2013; Rheuban et al., 2014a). The area of integration, or footprint, increases with height, but large footprints are generally considered beneficial as they integrate benthic heterogeneity (Rheuban & Berg 2013). Greater heights also increase the time-lag for changes at the benthic surface to reach the measurement point, but this can be corrected when correlating fluxes to environmental driving variables (i.e., irradiance, tides, concentrations) (Rheuban & Berg 2013). Further, the effects of these potential biases can be reduced by increasing deployment duration, especially over a variety of nonsteady state conditions, to better integrate flux estimates through time (Holtappels et al., 2013). Therefore, considering the substantial benefit of sampling higher above the bottom to remove wave bias, and the lower risk of other factors above, it is recommended to use adequate measurement heights (e.g., Figure 7b) at shallow sites where waves may be present.

4.6. Application to Similar Flux Techniques

The gradient flux, or profile flux, technique relies on the same boundary layer assumptions as the EC technique, but uses measurements of the gradient or profile of current velocity and solute concentrations through the boundary layer (McGillis et al., 2009, 2011; Takeshita et al., 2016; Turk et al., 2016). Similar to the development of aquatic EC, the scalar transport of gas and water fluxes in the marine atmospheric boundary layer steered these developments (Edson et al., 2004; McGillis et al., 2001; Zappa et al., 2003). In the gradient flux technique, the flux of a solute is calculated as:

$$Flux = -K_z \frac{\partial C}{\partial z} \tag{7}$$

where $-K_z$ is the eddy diffusivity, and $\frac{\partial C}{\partial z}$ is the benthic concentration gradient usually measured using a pair of chemical sensors or a dual-height pumping system at known heights (z) above the bottom (Takeshita et al., 2016). Gradient exchange fluxes are determined by taking the integral of Equation 7 across ∂z and using the relationship $K_z = u^* \kappa z$ (where u^* is the friction velocity and κ is Von Karman's constant) (McGillis et al., 2009). The resulting relationship [$Flux = u^* \kappa \left(\left(C_{z_2} - C_{z_1} \right) / \log \left(z_2 / z_1 \right) \right)$] makes use of u^* determined from logarithmic fits to benthic current profiles, which is an assumption that is often problematic in high roughness shallow systems during low flow conditions in the presence of waves (Davis et al., 2020). The gradient exchange technique has been primarily applied in shallow coastal seagrass and reef ecosystems (McGillis et al., 2009; Takeshita et al., 2016; Turk et al., 2016) and could benefit from the new analysis framework applied here by the direct calculation of K_z. Assuming a Prandtl number of 1, the eddy diffusivity can be calculated by:

$$K_z = \left(\overline{u'w'} \right) / \frac{\partial U}{\partial z} \tag{8}$$

where $\left(\overline{u'w'} \right)$ is the momentum flux (e.g., Equation 1) and $\frac{\partial U}{\partial z}$ is the shear calculated from a velocity profile of mean flow (Holtappels & Lorke, 2011). Using the CPSD accumulation for determining the momentum fluxes will yield direct measurements of K_z, which is superior to the assumption of a logarithmic boundary layer current profile (Holtappels & Lorke, 2011), especially in high-roughness shallow environments such as shallow-water coral reefs and seagrass beds where flow profiles often do not follow a logarithmic relationship (Davis et al., 2020; Nepf, 2012). For example, the momentum fluxes calculated from traditional covariance analysis produced substantially larger values (Table 2, Figure 4) and accumulating the CPSD below the wave frequencies will enable a more accurate determination of K_z for the gradient exchange technique while removing the need to assume a logarithmic boundary layer current profile.

5. Summary

The review of aquatic biogeochemical EC literature has revealed that biases created by waves have complicated the use of aquatic EC in shallow waters at a time when coastal processes are gaining recognition as important factors in nearshore water quality, regional biogeochemical cycles and global modeling efforts. However, the conditions and instrument configurations used during previous shallow-water studies where waves were present suggests that a change in how EC measurements are conducted and analyzed can overcome these limitations. The new analysis framework presented here, including using appropriate measurement heights and CPSD accumulation up to wave frequencies, demonstrates and that full-spectrum CPSD analysis is consistent with traditional EC analysis, and that wave-bias apparent in traditional EC analysis can be removed through exclusion of waves frequencies using spectral CPSD accumulation. By using the new approaches presented here (spectral filtering, microfluidics, rotating instrument) turbulent fluxes can be determined without contamination from current velocities, surface waves, or bias due to sensor separation. The spectral analysis framework can also be applied to standard EC and gradient exchange systems to

reduce the bias created by wave-sensitive sensors and bias in turbulence and velocity measurements. The application of the presented spectral analysis framework requires measurements to be conducted at sufficient heights from the interface, and also has the significant benefit of allowing for chemical sensors with slower response times, enabling new sensor and tracer applications to the EC technique.

Data Availability Statement

Data for this study are archived at the Biological & Chemical Oceanography Data Management Office per NSF policies (https://www.bco-dmo.org/person/560155).

Acknowledgments
This work benefitted from numerous discussions with Malcolm Scully, John Trowbridge, Jennie Rheuban, Wade McGillis, and the wider aquatic EC community, in general. The manuscript was improved substantially by reviewers, especially by Geno Pawlak. We thank Jennie Rheuban, Daniel McCorkle, Brian Hopkinson, and Kyle Conner for assistance with field work. This work was supported by the Independent Research & Development Program at WHOI and NSF OCE grants 1657727 and 1633951. The author declares no conflict of interest.

References

Amador, A., Giddings, S. G., & Pawlak, G. (2020). *ADCP-based estimates of lateral turbulent Reynolds stresses in wavy coastal environments*. https://doi.org/10.13140/RG.2.2.21700.65924

Attard, K. M., Glud, R. N., McGinnis, D. F., & Rysgaard, S. (2014). Seasonal rates of benthic primary production in a Greenland fjord measured by aquatic eddy correlation. *Limnology & Oceanography*, *59*(5), 1555–1569. https://doi.org/10.4319/lo.2014.59.5.1555

Attard, K. M., Hancke, K., Sejr, M. K., & Glud, R. N. (2016). Benthic primary production and mineralization in a High Arctic fjord: In situ assessments by aquatic eddy covariance. *Marine Ecology Progress Series*, *554*, 35–50.

Attard, K. M., Rodil, I. F., Glud, R. N., Berg, P., Norkko, J., & Norkko, A. (2019). Seasonal ecosystem metabolism across shallow benthic habitats measured by aquatic eddy covariance. *Limnology and Oceanography Letters*, *4*(3), 79–86. https://doi.org/10.1002/lol2.10107

Attard, K. M., Søgaard, D. H., Piontek, J., Lange, B. A., Katlein, C., Sørensen, H. L., et al.(2018). Oxygen fluxes beneath Arctic land-fast ice and pack ice: Towards estimates of ice productivity. *Polar Biology*, *41*(10), 2119–2134.

Attard, K. M., Stahl, H., Kamenos, N. A., Turner, G., Burdett, H. L., & Glud, R. N. (2015). Benthic oxygen exchange in a live coralline algal bed and an adjacent sandy habitat: An eddy covariance study. *Marine Ecology Progress Series*, *535*, 99–115.

Baldocchi, D. D. (2003). Assessing the eddy covariance technique for evaluating carbon dioxide exchange rates of ecosystems: past, present and future. *Global Change Biology*, *9*, 479–492. https://doi.org/10.1046/j.1365-2486.2003.00629.x

Benilov, A. Y., & Filyushkin, B. N. (1970). Application of methods of linear filtration to an analysis of fluctuations in the surface layer of the sea. *Izvestiya: Atmospheric and Oceanic Physics*, *6*, 810–819.

Berg, P., Delgard, M. L., Polsenaere, P., McGlathery, K. J., Doney, S. C., & Berger, A. C. (2019). Dynamics of benthic metabolism, O_2, and pCO_2 in a temperate seagrass meadow. *Limnology & Oceanography*, *64*(6), 2586–2604.

Berger, A. C., Berg, P., McGlathery, K. J., & Delgard, M. L. (2020). Long-term trends and resilience of seagrass metabolism: A decadal aquatic eddy covariance study. *Limnology & Oceanography*.

Berg, P., Glud, R. N., Hume, A., Stahl, H., Oguri, K., Meyer, V., & Kitazato, H. (2009). Eddy correlation measurements of oxygen uptake in deep ocean sediments. *Limnology and Oceanography: Methods*, *7*(8), 576–584. https://doi.org/10.4319/lom.2009.7.576

Berg, P., & Huettel, M. (2008). Monitoring the seafloor using the noninvasive eddy correlation technique. *Oceanography*, *21*(4), 164–167.

Berg, P., Koopmans, D. J., Huettel, M., Li, H., Mori, K., & Wüest, A., 2016. A new robust oxygen-temperature sensor for aquatic eddy covariance measurements. *Limnology and Oceanography: Methods*, *14*(3), 151–167. https://doi.org/10.1002/lom3.10071

Berg, P., Long, M. H., Huettel, M., Rheuban, J. E., McGlathery, K. J., Howarth, R. W., et al. (2013). Eddy correlation measurements of oxygen fluxes in permeable sediments exposed to varying current flow and light. *Limnology & Oceanography*, *58*(4), 1329–1343.

Berg, P., & Pace, M. L., 2017. Continuous measurement of air–water gas exchange by underwater eddy covariance. *Biogeosciences*, *14*(23), 5595–5606. https://doi.org/10.5194/bg-14-5595-2017

Berg, P., Reimers, C. E., Rosman, J., Özkan-Haller, T., Huettel, M., & Delgard, M. L. (2015). Technical Note: Time lag correction of aquatic eddy covariance data measured in the presence of waves. *Biogeosciences Discussions*, *12*, 8395–8427. https://doi.org/10.5194/bgd-12-8395-2015

Berg, P., Røy, H., Janssen, F., Meyer, V., Jørgensen, B., Huettel, M., & de Beer, D. (2003). Oxygen uptake by aquatic sediments measured with a novel non-invasive eddy-correlation technique. *Marine Ecology Progress Series*, *261*, 75–83. https://doi.org/10.3354/meps261075

Bittig, H. C., Fiedler, B., Scholz, R., Krahmann, G., & Körtzinger, A. (2014). Time response of oxygen optodes on profiling platforms and its dependence on flow speed and temperature. *Limnology and Oceanography: Methods*, *12*(8), 617–636.

Brand, A., McGinnis, D. F., Wehrli, B., & Wuest, A. (2008). Intermittent oxygen flux from the interior into the bottom boundary of lakes as observed by eddy correlation. *Limnology & Oceanography*, *53*(5), 1997–2006.

Bricker, J. D., & Monismith, S. G. (2007). Spectral wave–turbulence decomposition. *Journal of Atmospheric and Oceanic Technology*, *24*(8), 1479–1487.

Burba, G., & Anderson, D. (2010). *A brief practical guide to eddy covariance flux measurements: Principles and workflow examples for scientific and industrial applications*. Lincoln, NE, USA: LI-COR Biosciences http://www.licor.com/eddycovariance

Cathalot, C., Oevelen, D. V., Cox, T. J., Kutti, T., Lavaleye, M. S., Duineveld, G. C., & Meysman, F. J. (2015). Cold-water coral reefs and adjacent sponge grounds: Hotspots of benthic respiration and organic carbon cycling in the deep sea. *Frontiers in Marine Science*, *2*, 1–12.

Chipman, L., Huettel, M., Berg, P., Meyer, V., Klimant, I., Glud, R., & Wenzhoefer, F. (2012). Oxygen optodes as fast sensors for eddy correlation measurements in aquatic systems. *Limnology and Oceanography: Methods*, *10*(5), 304–316.

Crusius, J., Berg, P., Koopmans, D. J., & Erban, L. (2008). Eddy correlation measurements of submarine groundwater discharge. *Marine Chemistry*, *109*(1–2), 77–85.

Cyronak, T., Santos, I. R., McMahon, A., & Eyre, B. D., 2013. Carbon cycling hysteresis in permeable carbonate sands over a diel cycle: Implications for ocean acidification. *Limnology & Oceanography*, *58*(1), 131–143. https://doi.org/10.4319/lo.2013.58.1.0131

Davis, K. A., Pawlak, G., & Monismith, S. G. (2020). Turbulence and coral reefs. *Annual Review of Marine Science*, *13*, 343–373.

de Froe, E., Rovelli, L., Glud, R. N., Maier, S. R., Duineveld, G., Mienis, F., et al. (2019). Benthic oxygen and nitrogen exchange on a cold-water coral reef in the North-East Atlantic Ocean. *Frontiers in Marine Science*, *6*, 665.

Donis, D., Holtappels, M., Noss, C., Cathalot, C., Hancke, K., Polsenaere, P., & McGinnis, D. F. (2015). An assessment of the precision and confidence of aquatic eddy correlation measurements. *Journal of Atmospheric and Oceanic Technology*, *32*(3), 642–655. https://doi.org/10.1175/JTECH-D-14-00089.1

Donis, D., McGinnis, D. F., Holtappels, M., Felden, J., & Wenzhoefer, F. (2016). Assessing benthic oxygen fluxes in oligotrophic deep sea sediments (HAUSGARTEN observatory). *Deep Sea Research Part I: Oceanographic Research Papers*, *111*, 1–10.

Duarte, C. M., Marbà, N., Gacia, E., Fourqurean, J. W., Beggins, J., Barrón, C. & Apostolaki, E. T. (2010). Seagrass community metabolism: Assessing the carbon sink capacity of seagrass meadows. *Global Biogeochemical Cycles*, *24*(4), GB4032. https://doi.org/10.1029/2010GB003793

Edson, J. B., Hinton, A. A., Prada, K. E., Hare, J. E., & Fairall, C. W. (1998). Direct covariance flux estimates from mobile platforms at sea. *Journal of Atmospheric and Oceanic Technology*, *15*(2), 547–562. https://doi.org/10.1175/1520-0426(1998)015<0547:DCFEFM>2.0.CO;2

Edson, J. B., Zappa, C. J., Ware, J. A., McGillis, W. R. & Hare, J. E. (2004). Scalar flux profile relationships over the open ocean. *Journal of Geophysical Research: Oceans*, *109*(C8), C08S09. https://doi.org/10.1029/2003JC001960

Else, B. G. T., Rysgaard, S., Attard, K., Campbell, K., Crabeck, O., Galley, R. J., et al. (2015). Under-ice eddy covariance flux measurements of heat, salt, momentum, and dissolved oxygen in an artificial sea ice pool. *Cold Regions Science and Technology*, *119*, 158–169.

Fairall, C. W., Hare, J. E., Edson, J. B., & McGillis, W. (2000). Parameterization and micrometeorological measurement of air–sea gas transfer. *Boundary-Layer Meteorology*, *96*(1–2), 63–106.

Flügge, M., Paskyabi, M. B., Reuder, J., Edson, J. B., & Plueddemann, A. J. (2016). Comparison of Direct Covariance Flux Measurements from an Offshore Tower and a Buoy. *Journal of Atmospheric and Oceanic Technology*, *33*(5), 873–890. https://doi.org/10.1175/JTECH-D-15-0109.1

Gerbi, G. P., Trowbridge, J. H., Edson, J. B., Plueddemann, A. J., Terray, E. A. & Fredericks, J. J. (2008). Measurements of momentum and heat transfer across the air–sea interface. *Journal of Physical Oceanography*, *38*(5), 1054–1072. https://doi.org/10.1175/2007JPO3739.1

Glud, R. N., Berg, P., Hume, A., Batty, P., Blicher, M. E., Lennert, K., & Rysgaard, S. (2010). Benthic O2 exchange across hard-bottom substrates quantified by eddy correlation in a sub-Arctic fjord. *Marine Ecology Progress Series*, *417*, 1–12.

Glud, R. N., Berg, P., Stahl, H., Hume, A., Larsen, M., Eyre, B. D., & Cook, P. L. (2016). Benthic carbon mineralization and nutrient turnover in a Scottish sea loch: an integrative in situ study. *Aquatic Geochemistry*, *22*(5–6), 443–467.

Glud, R. N., Rysgaard, S., Turner, G., McGinnis, D. F., & Leakey, R. J. (2014). Biological-and physical-induced oxygen dynamics in melting sea ice of the Fram Strait. *Limnology & Oceanography*, *59*(4), 1097–1111.

Goring, D. G., & Nikora, V. I. (2002). Despiking acoustic doppler velocimeter data. *Journal of Hydraulic Engineering*, *128*(1), 117–126. https://doi.org/10.1061/(asce)0733-9429(2002)128:1(117)

Holtappels, M., Glud, R. N., Donis, D., Liu, B., Hume, A., Wenzhöfer, F. & Kuypers, M. M. (2013). Effects of transient bottom water currents and oxygen concentrations on benthic exchange rates as assessed by eddy correlation measurements. *Journal of Geophysical Research: Oceans*, *118*(3), 1157–1169. https://doi.org/10.1002/jgrc.20112

Holtappels, M., & Lorke, A. (2011). Estimating turbulent diffusion in a benthic boundary layer. *Limnology and Oceanography: Methods*, *9*(1), 29–41.

Holtappels, M., Noss, C., Hancke, K., Cathalot, C., McGinnis, D. F., Lorke, A., & Glud, R. N. (2015). Aquatic Eddy Correlation: Quantifying the Artificial Flux Caused by Stirring-Sensitive O_2 Sensors. *PloS One*, *10*(1), e0116564. https://doi.org/10.1371/journal.pone.0116564

Hopkinson, B. M., King, A. C., Johnson-Roberson, M., Long, M. H., & Bhandarkar, M. (2020). Automated classification of three-dimensional reconstructions of coral reefs using convolutional neural networks. *PloS One*, *15*(3), e0230671. https://doi.org/10.1371/journal.pone.0230671

Hume, A., Berg, P., & McGlathery, K. J. (2011). Dissolved oxygen fluxes and ecosystem metabolism in an eelgrass (*Zostera marina*) meadow measured with the novel eddy correlation technique. *Limnology & Oceanography*, *56*, 86–96.

Johnson, K. S., Barry, J. P., Coletti, L. J., Fitzwater, S. E., Jannasch, H. W., & Lovera, C. F. (2011). Nitrate and oxygen flux across the sediment-water interface observed by eddy correlation measurements on the open continental shelf. *Limnology and Oceanography: Methods*, *9*(11), 543–553.

Kaimal, J. C., Wyngaard, J. C. J., Izumi, Y., & Coté, O. R. (1972). Spectral characteristics of surface-layer turbulence. *Quarterly Journal of the Royal Meteorological Society*, *98*(417), 563–589.

Kirincich, A. R., Lentz, S. J., & Gerbi, G. P. (2010). Calculating Reynolds stresses from ADCP measurements in the presence of surface gravity waves using the cospectra-fit method. *Journal of Atmospheric and Oceanic Technology*, *27*(5), 889–907.

Klimant, I., Meyer, V., & Kühl, M. (1995). Fiber-optic oxygen microsensors, a new tool in aquatic biology. *Limnology & Oceanography*, *40*(6), 1159–1165.

Koopmans, D. J., & Berg, P. (2015). Stream oxygen flux and metabolism determined with the open water and aquatic eddy covariance techniques. *Limnology & Oceanography*, *60*(4), 1344–1355.

Koopmans, D., Holtappels, M., Chennu, A., Weber, M., & de Beer, D. (2020). High net primary production of Mediterranean seagrass (*Posidonia oceanica*) meadows determined with aquatic eddy covariance. *Frontiers in Marine Science*, *7*, 118. https://doi.org/10.3389/fmars.2020.00118

Kreling, J., Bravidor, J., McGinnis, D. F., Koschorreck, M. & Lorke, A., 2014. Physical controls of oxygen fluxes at pelagic and benthic oxyclines in a lake. *Limnology & Oceanography*, *59*(5), 1637–1650. https://doi.org/10.4319/lo.2014.59.5.1637

Kuwae, T., Kamio, K., Inoue, T., Miyoshi, E., & Uchiyama, Y. (2006). Oxygen exchange flux between sediment and water in an intertidal sandflat, measured in situ by the eddy-correlation method. *Marine Ecology Progress Series*, *307*, 59–68.

Lee, J. S., Kang, D. J., Hineva, E., Slabakova, V., Todorova, V., Park, J., & Cho, J. H. (2017). Estimation of net ecosystem metabolism of seagrass meadows in the coastal waters of the East Sea and Black Sea using the noninvasive eddy covariance technique. *Ocean Science Journal*, *52*(2), 243–256.

Lee, X.,Massman, W.,& Law,B.(Eds.), (2004). *Handbook of micrometeorology: A guide for surface flux measurement and analysis*. Springer-Verlag.

Long, M. H., Berg, P., de Beer, D., & Zieman, J. C. (2013). In situ coral reef oxygen metabolism: an eddy correlation study. *PloS One*, *8*(3), e58581. https://doi.org/10.1371/journal.pone.0058581

Long, M. H., Berg, P., & Falter, J. L. (2015c). Seagrass metabolism across a productivity gradient using the eddy covariance, Eulerian control volume, and biomass addition techniques. *Journal of Geophysical Research: Oceans*, *120*(5), 3624–3639. https://doi.org/10.1002/2014JC010352

Long, M. H., Berg, P., McGlathery, K. J., & Zieman, J. C. (2015b). Sub-tropical seagrass ecosystem metabolism measured by eddy covariance. *Marine Ecology Progress Series*, *529*, 75–90. https://doi.org/10.3354/meps11314

Long, M. H., Charette, M. A., Martin, W. R., & McCorkle, D. C. (2015a). Oxygen metabolism and pH in coastal ecosystems: Eddy Covariance Hydrogen ion and Oxygen Exchange System (ECHOES). *Limnology and Oceanography: Methods*, *13*(8), 438–450. https://doi.org/10.1002/lom3.10038

Long, M. H., Koopmans, D., Berg, P., Rysgaard, S., Glud, R. N., & Søgaard, D. H. (2012a). Oxygen exchange and ice melt measured at the ice-water interface by eddy correlation. *Biogeosciences*, *9*(6), 1957–1967. https://doi.org/10.5194/bg-9-1957-2012

Long, M. H. & Nicholson, D. P. (2018). Surface gas exchange determined from an aquatic eddy covariance floating platform. *Limnology and Oceanography: Methods*, *16*(3), 145–159. https://doi.org/10.1002/lom3.10233

Long, M. H., Rheuban, J. E., Berg, P., & Zieman, J. C. (2012b). A comparison and correction of light intensity loggers to photosynthetically active radiation sensors. *Limnology and Oceanography: Methods*, *10*(6), 416–424.

Long, M. H., Rheuban, J. E., McCorkle, D. C., Burdige, D. J. & Zimmerman, R. C. (2019). Closing the oxygen mass balance in shallow coastal ecosystems. *Limnology & Oceanography*, *64*(6), 2694–2708. https://doi.org/10.1002/lno.11248

Long, M. H., Sutherland, K., Wankel, S. D., Burdige, D. J. & Zimmerman, R. C., 2020. Ebullition of oxygen from seagrasses under supersaturated conditions. *Limnology & Oceanography*, *65*(2), 314–324. https://doi.org/10.1002/lno.11299

Lorke, A., McGinnis, D. F., & Maeck, A. (2013). Eddy-correlation measurements of benthic fluxes under complex flow conditions: Effects of coordinate transformations and averaging time scales. *Limnology and Oceanography: Methods*, *11*(8), 425–437.

Lorke, A., McGinnis, D. F., Maeck, A., & Fischer, H. (2012). Effect of ship locking on sediment oxygen uptake in impounded rivers. *Water Resources Research*, *48*(12), W12514.

Lorrai, C., McGinnis, D. F., Berg, P., Brand, A., & Wüest, A. (2010). Application of oxygen eddy correlation in aquatic systems. *Journal of Atmospheric and Oceanic Technology*, *27*(9), 1533–1546.

Lumley, J. L., & Terray, E. A. (1983). Kinematics of turbulence convected by a random wave field. *Journal of Physical Oceanography*, *13*(11), 2000–2007.

Martz, T. R., Connery, J. G., & Johnson, K. S. (2010). Testing the Honeywell Durafet® for seawater pH applications. *Limnology and Oceanography: Methods*, *8*(5), 172–184.

McCann-Grosvenor, K., Reimers, C. E., & Sanders, R. D. (2014). Dynamics of the benthic boundary layer and seafloor contributions to oxygen depletion on the Oregon inner shelf. *Continental Shelf Research*, *84*, 93–106.

McGillis, W. R., Edson, J. B., Hare, J. E., & Fairall, C. W. (2001). Direct covariance air-sea CO_2 fluxes. *Journal of Geophysical Research: Oceans*, *106*(C8), 16729–16745. https://doi.org/10.1029/2000JC000506

McGillis, W. R., Langdon, C., Loose, B., Yates, K. K., & Corredor, J. (2011). Productivity of a coral reef using boundary layer and enclosure methods. *Geophysical Research Letters*, *38*, L03611. https://doi.org/10.1029/2010GL046179

McGillis, W. R., Langdon, C., Williams, A. J., & Loose, B. (2009). *O2 MAVS: an Instrument for Measuring Oxygen Flux. MTS/IEEE Biloxi - Marine technology for our future: Global and local challenges*, 2009 No. 5422166. OCEANS.

McGinnis, D. F., Berg, P., Brand, A., Lorrai, C., Edmonds, T. J., & Wüest, A. (2008). Measurements of eddy correlation oxygen fluxes in shallow freshwaters: Towards routine applications and analysis. *Geophysical Research Letters*, *35*(4), L04403. https://doi.org/10.1029/2007GL032747

McGinnis, D. F., Cherednichenko, S., Sommer, S., Berg, P., Rovelli, L., Schwarz, R., et al. (2011). Simple, robust eddy correlation amplifier for aquatic dissolved oxygen and hydrogen sulfide flux measurements. *Limnology and Oceanography: Methods*, *9*(8), 340–347.

McGinnis, D. F., Sommer, S., Lorke, A., Glud, R. N., & Linke, P. (2014). Quantifying tidally driven benthic oxygen exchange across permeable sediments: An aquatic eddy correlation study. *Journal of Geophysical Research: Oceans*, *119*(10), 6918–6932.

Muehllehner, N., Langdon, C., Venti, A., & Kadko, D. (2016). Dynamics of carbonate chemistry, production, and calcification of the Florida Reef Tract (2009–2010): Evidence for seasonal dissolution. *Global Biogeochemical Cycles*, *30*(5), 661–688. https://doi.org/10.1002/2015GB005327

Murniati, E., Geissler, S., & Lorke, A. (2015). Short-term and seasonal variability of oxygen fluxes at the sediment–water interface in a riverine lake. *Aquatic Sciences*, *77*(2), 183–196.

Nepf, H. M. (2012). Flow and transport in regions with aquatic vegetation. *Annual Review of Fluid Mechanics*, *44*(2012), 123–142. https://doi.org/10.1146/annurev-fluid-120710-101048

Owen, D. P., Long, M. H., Fitt, W. K., & Hopkinson, B. M. (2020). Taxon-specific primary production rates on coral reefs in the Florida Keys. *Limnology & Oceanography*. https://doi.org/10.1002/lno.11627

Plew, D. R. (2019). Investigating benthic impacts at salmon farms using eddy covariance measurements of benthic oxygen fluxes. *Aquaculture Environment Interactions*, *11*, 337–357.

Reidenbach, M. A., Berg, P., Hume, A., Hansen, J. C., & Whitman, E. R. (2013). Hydrodynamics of intertidal oyster reefs: The influence of boundary layer flow processes on sediment and oxygen exchange. *Limnology and Oceanography: Fluids and Environments*, *3*(1), 225–239.

Reimers, C. E., Özkan-Haller, H. T., Albright, A. T., & Berg, P. (2016a). Microelectrode velocity effects and aquatic eddy covariance measurements under waves. *Journal of Atmospheric and Oceanic Technology*, *33*(2), 263–282.

Reimers, C. E., Özkan-Haller, H. T., Sanders, R. D., McCann-Grosvenor, K., Chace, P. J., & Crowe, S. A. (2016b). The dynamics of benthic respiration at a mid-shelf station off Oregon. *Aquatic Geochemistry*, *22*(5–6), 505–527.

Reimers, C. E., Özkan-Haller, H., Berg, P., Devol, A., McCann-Grosvenor, K., & Sanders, R. D. (2012). Benthic oxygen consumption rates during hypoxic conditions on the Oregon continental shelf: Evaluation of the eddy correlation method. *Journal of Geophysical Research: Oceans*, *117*(C2), C02021. https://doi.org/10.1029/2011JC007564

Revsbech, N. P. (1989). An oxygen microsensor with a guard cathode. *Limnology & Oceanography*, *34*(2), 474–478.

Rheuban, J. E., & Berg, P. (2013). The effects of spatial and temporal variability at the sediment surface on aquatic eddy correlation flux measurements. *Limnology Oceanography Methods*, *11*, 351–359.

Rheuban, J. E., Berg, P., & McGlathery, K. J. (2014a). Multiple timescale processes drive ecosystem metabolism in eelgrass (*Zostera marina*) meadows. *Marine Ecology Progress Series*, *507*, 1–13.

Rheuban, J. E., Berg, P., & McGlathery, K. J. (2014b). Ecosystem metabolism along a colonization gradient of eelgrass (*Zostera marina*) measured by eddy correlation. *Limnology & Oceanography*, *59*(4), 1376–1387.

Rodil, I. F., Attard, K. M., Norkko, J., Glud, R. N., & Norkko, A. (2019). Towards a sampling design for characterizing habitat-specific benthic biodiversity related to oxygen flux dynamics using Aquatic Eddy Covariance. *PloS One*, *14*(2), e0211673.

Rosman, J. H., & Gerbi, G. P. (2017). Interpreting fixed-location observations of turbulence advected by waves: Insights from spectral models. *Journal of Physical Oceanography*, *47*(4), 909–931.

Rovelli, L., Attard, K. M., Binley, A., Heppell, C. M., Stahl, H., Trimmer, M., & Glud, R. N. (2017). Reach-scale river metabolism across contrasting sub-catchment geologies: Effect of light and hydrology. *Limnology & Oceanography*, *62*(S1), S381–S399.

Rovelli, L., Attard, K. M., Bryant, L. D., Flögel, S., Stahl, H., Roberts, J. M., et al. (2015). Benthic O2 uptake of two cold-water coral communities estimated with the non-invasive eddy correlation technique. *Marine Ecology Progress Series*, *525*, 97–104.

Rovelli, L., Attard, K. M., Cárdenas, C. A., & Glud, R. N. (2019). Benthic primary production and respiration of shallow rocky habitats: a case study from South Bay (Doumer Island, Western Antarctic Peninsula). *Polar Biology*, *42*(8), 1459–1474.

Rovelli, L., Attard, K. M., Heppell, C. M., Binley, A., Trimmer, M., & Glud, R. N. (2018). Headwater gas exchange quantified from O_2 mass balances at the reach scale. *Limnology and Oceanography: Methods*, *16*(10), 696–709.

Santos, I. R., Glud, R. N., Maher, D., Erler, D., & Eyre, B. D. (2011). Diel coral reef acidification driven by porewater advection in permeable carbonate sands, Heron Island, Great Barrier Reef. *Geophysical Research Letters*, *38*(3). https://doi.org/10.1029/2010GL046053

Scully, M. E., Trowbridge, J. H., & Fisher, A. W. (2016). Observations of the transfer of energy and momentum to the oceanic surface boundary layer beneath breaking waves. *Journal of Physical Oceanography*, *46*(6), 1823–1837. https://doi.org/10.1175/JPO-D-15-0165.1

Shaw, W. J., & Trowbridge, J. H. (2001). The direct estimation of near-bottom turbulent fluxes in the presence of energetic wave motions. *Journal of Atmospheric and Oceanic Technology*, *18*(9), 1540–1557.

Stacey, M. T., Monismith, S. G., & Burau, J. R. (1999). Measurements of Reynolds stress profiles in unstratified tidal flow. *Journal of Geophysical Research: Oceans*, *104*(C5), 10933–10949.

Swinbank, W. C. (1951). The measurement of vertical transfer of heat and water vapor by eddies in the lower atmosphere. *Journal of Meteorology*, *8*(3), 135–145.

Takeshita, Y., McGillis, W. R., Briggs, E. M., Carter, A. L., Donham, E. M., & Martz, T. R. (2016). Assessment of net community production and calcification of a coral reef using a boundary layer approach. *Journal of Geophysical Research: Oceans*, *121*(8), 5655–5671. doi:10.1002/2016JC011886

Trowbridge, J. H. (1998). On a technique for measurement of turbulent shear stress in the presence of surface waves. *Journal of Atmospheric and Oceanic Technology*, *15*(1), 290–298.

Trowbridge, J., Scully, M. and Sherwood, C. R., 2018. The cospectrum of stress-carrying turbulence in the presence of surface gravity waves. *Journal of Physical Oceanography*, *48*(1), 29–44. https://doi.org/10.1175/JPO-D-17-0016.1

Turk, D., Bedard, J. M., Burt, W. J., Vagle, S., Thomas, H., Azetsu-Scott, K., & McGillis, W. R. (2016). Inorganic carbon in a high latitude estuary-fjord system in Canada's eastern Arctic. *Estuarine. Coastal and Shelf Science*, *178*, 137–147.

Volaric, M. P., Berg, P., & Reidenbach, M. A. (2018). Oxygen metabolism of intertidal oyster reefs measured by aquatic eddy covariance. *Marine Ecology Progress Series*, *599*, 75–91.

Volaric, M. P., Berg, P., & Reidenbach, M. A. (2019). An invasive macroalga alters ecosystem metabolism and hydrodynamics on a tidal flat. *Marine Ecology Progress Series*, *628*, 1–16.

Volaric, M. P., Berg, P., & Reidenbach, M. A. (2020). Drivers of oyster reef ecosystem metabolism measured across multiple timescales. *Estuaries and Coasts*, *43*, 2034–2045.

Weck, J., & Lorke, A., 2017. Mixing efficiency in the thermocline of lakes observed from eddy correlation flux measurements. *Journal of Geophysical Research: Oceans*, *122*(1), 291–305. https://doi.org/10.1002/2016JC012188

Wyngaard, J. C., & Coté, O. R. (1972). Cospectral similarity in the atmospheric surface layer. *Quarterly Journal of the Royal Meteorological Society*, *98*(417), 590–603.

Yamamoto, S., Kayanne, H., Tokoro, T., Kuwae, T., & Watanabe, A. (2015). Total alkalinity flux in coral reefs estimated from eddy covariance and sediment pore-water profiles. *Limnology & Oceanography*, *60*(1), 229–241.

Zappa, C. J., Raymond, P. A., Terray, E. A., & McGillis, W. R. (2003). Variation in surface turbulence and the gas transfer velocity over a tidal cycle in a macro-tidal estuary. *Estuaries*, *26*(No. 6), 1401–1415.